ACTINIDE RESEARCH QUARTERLY

Ac Th Pa U Np Pu Am Cm Bk Cf Es Fm Md No Lr

Second Quarter 2020

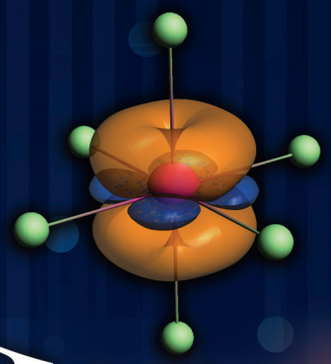

$$H(t)|\psi(t)\rangle = i\hbar\frac{\partial}{\partial t}|\psi(t)\rangle$$

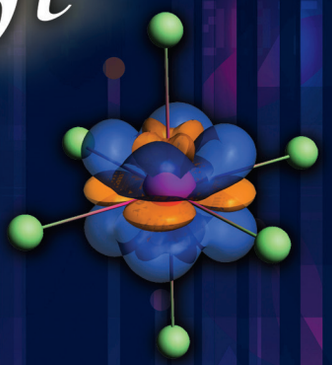

Theory and simulation

ACTINIDE SCIENCE TO BREAK THROUGH

Los Alamos
NATIONAL LABORATORY
EST. 1943

Foreword

Accurately predicting the properties of actinide systems is one of the greatest challenges in computational science today. Many advances have been made in the last few decades thanks to improvements in computing hardware and algorithms, and to new developments in electron correlation methods and the treatment of relativistic effects. This progress enables complicated calculations that are realistic and leads to exciting new approaches in areas such as electronic spectroscopy, magnetism, dynamic behavior, and surface reactivity. Nevertheless, there remains much potential to further improve our predictive power ranging from extended systems (e.g., strongly-correlated materials) to the discrete level (e.g., the chemical behavior of actinide-containing molecules).

The **Theory Frontiers in Actinide Sciences: Chemistry and Materials** workshop was held in Santa Fe, New Mexico, February 2–4, 2020, organized by the G.T. Seaborg Institute and the Center for Nonlinear Studies at Los Alamos National Laboratory (LANL). We discussed the scientific challenges faced today by the physics, chemistry, and materials science research communities. Insights into these phenomena were shared from different perspectives with the hope of building new collaborations and developing new ideas for tackling these problems. A half-day tutorial session kicked off the workshop, covering three distinctive research areas: Art Voter (LANL) introduced accelerated molecular dynamics methods for the study of rare-event pushing time scales beyond those reachable by standard molecular dynamics approaches, Xiaosong Li (University of Washington) presented an overview in the relativistic electronic structure, and Olle Eriksson (Uppsala University) showed how to calculate the magnetic properties of strongly correlated systems. In-depth discussions were facilitated by workshop sessions that brought together chemistry, physics, and materials actinide research communities from around the world. Each session opened with a presentation from an experimentalist in the field highlighting state-of-the-art data to challenge the theory community. The scope of the workshop encompassed both developments and applications of current methods in the study of 5f-element systems.

This special ARQ issue features six of the presentations from the workshop and highlights a variety of the different topics discussed. Clark (Washington State University) discusses advances in the theoretical treatment of actinide separations, an important area relevant to nuclear waste (p2). Andersson (LANL) meanwhile summarizes the impact of point defects in material properties relevant to the development of new nuclear fuels (p8). Lukens (Lawrence Berkeley National Laboratory) provides an introductory primer to actinide magnetic properties and the fascinating subject of single molecule magnetism (p14), and Wang's (LANL) article illustrates progress in surface chemistry modeling (p24). Goldman (Lawrence Livermore National Laboratory) highlights new advances in theoretical modeling of hydrogen reactions on delta plutonium surfaces (p31), and finally, Rosso (Pacific Northwest National Laboratory) describes the environmental mobility of uranium in terms of electron transfer reactions (p37).

Lastly, we would like to thank all participants for their excellent presentations and engaging discussions. The organizers would like to specially thank Susan Ramsay, Jenny Harvey, and Leah Bulnes for their administrative support to ensure a successful workshop. Last but not least, we are grateful for Owen Summerscales for his editing and proofing this special issue.

Organizers:

Ping Yang
G.T. Seaborg Institute

Enrique Batista
Center for Nonlinear Studies

Franz J. Freibert
G.T. Seaborg Institute

About the cover: The famous Schrödinger equation describes a quantum mechanical state of a system. In chemistry it can be used to describe the behavior of electrons in atoms and molecules, however it cannot be solved precisely for multi-electron atoms (i.e., most elements of the periodic table). Nevertheless, computational methods using iterative procedures allow us to approximate these solutions and produce data that can be mapped visually, such as shown with two molecular orbitals of uranium hexachloride. Advances in these techniques, and how they relate to experimental problems, were the subject of the *Theory Frontiers in Actinide Sciences: Chemistry and Materials* workshop held in Santa Fe, New Mexico in February of this year, and the focus of this issue of ARQ.

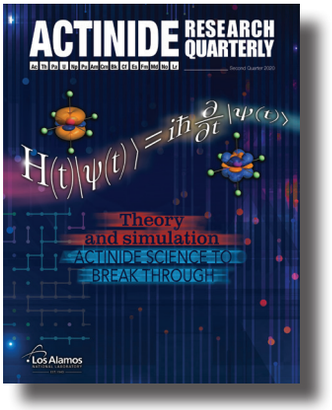

Contents

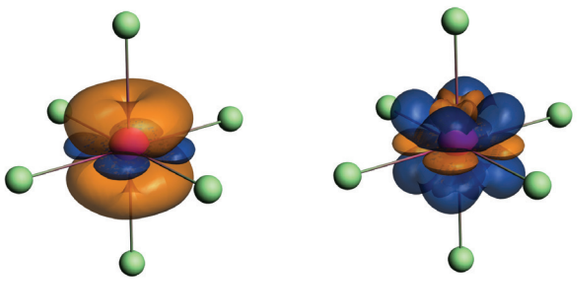

Actinide Separations

The fusion of data science, applied mathematics, and experimental chemistry is reviving the old technology of solvent extraction

Aurora Clark
Washington State University, Pullman, Washington

The ability to separate f-elements from complex mixtures is essential in many areas of applied actinide science. These include the nuclear power fuel cycle and radiotherapeutics, in which radioactive decay causes continuous changes to sample compositions. Liquid-liquid extraction (LLE) is a cornerstone technology of actinide separations, first introduced at the turn of the twentieth century and based upon the differential solubilities (or partitioning) of a solute between two immiscible liquid phases. It was used in the industrial-scale recovery and purification of plutonium during World War II and formed the basis for nuclear fuel recycling during the global-scale growth of nuclear energy. Although it is now completely integrated into the fabric of transuranic research, there remains a significant opportunity to increase efficiency and selectivity by developing a meaningful understanding of molecular scale behavior during the extraction process.

Actinide liquid-liquid extraction

In a single-stage separation, a complex aqueous mixture of solutes is mixed with an immiscible organic solvent and preferred solvation of one of the solutes occurs such that it migrates across the liquid/liquid phase boundary and into the organic phase (Fig. 1). Actinide separations often involve multiple stages in which pH is used to control the oxidation state, and thus coordination, of the actinide ions in the aqueous phase. Surface-active ligands can also be selective for certain metal ions in the mixture, based on their electronic structure. These ligands migrate to the liquid/liquid interface from the organic phase and undergo complexation reactions with interfacially-adsorbed ions that transform hydrophilic actinide ions into hydrophobic metal-ligand complexes which migrate into the organic phase. Thus, these ligands act as extractants, selectively separating actinide species from one phase to another. Among the many advancements to actinide LLE, a multitude of improvements in ligand design have been made which:

- Exhibit high selectivity
- Adhere to the CHON (carbon-hydrogen-oxygen-nitrogen) principle: Minimize waste volumes by using completely incinerable reagents
- Resist radiolytic degradation

These successes are remarkable given that the LLE process involves highly non-ideal solutions and potentially extreme chemical environments (e.g., low pH, high ionic strength). Despite this, LLE has been described historically using ideal chemical models in each of the key regions, namely: the aqueous phase, liquid/liquid interface, and the organic phase. The shortcomings of these models manifest themselves in a variety of interesting ways. For instance, interfacial metal-ligand species are generally assumed to be the same species observed in the organic phase with ideal coordination environments. This fails when one considers the deleterious phenomena of third-phase formation, in which metal-ligand complexes at the liquid/liquid phase boundary associate, forming aggregates or reverse micelles (i.e., aqueous droplets suspended in the organic phase) such that a new, metal-rich phase of higher density forms and splits from the lighter organic phase.

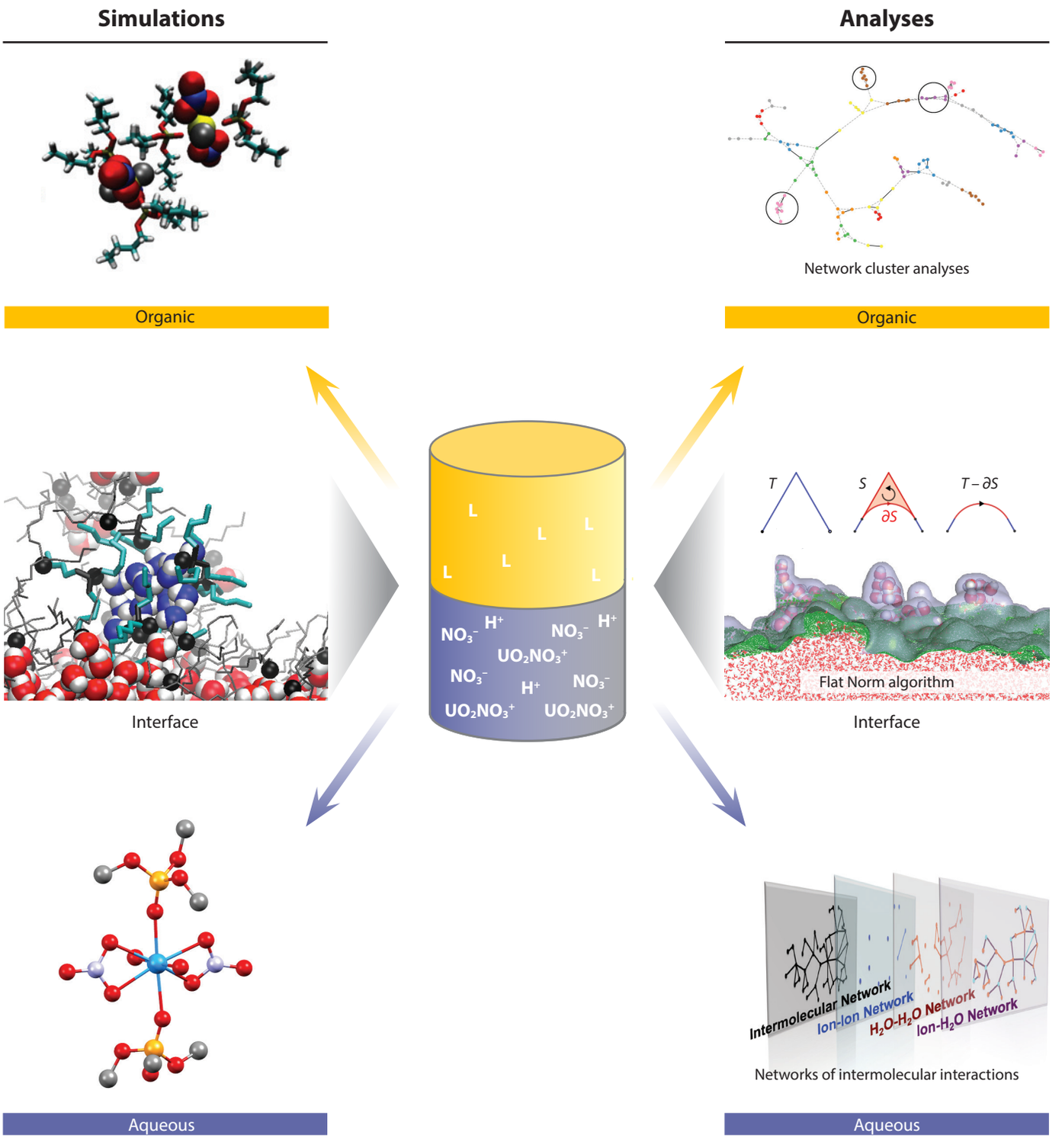

Figure 1. The center image represents a separation process used in a single stage solvent extraction reaction (L = ligand). *Left*: Images representative of the chemical species in the organic phase (*top*), the interface (*middle*), and the aqueous phase (*bottom*). *Right*: Analyses that reveal those chemical species and are discussed in the article; Network cluster analyses (*top*) for the organic phase, the Flat Norm algorithm for the interface (*middle*), and the networks of intermolecular interactions that are applied to understand aqueous phase speciation (*bottom*).

Understanding the non-ideality of LLE is key to the next stage in the development of this old technology which will help prevent undesirable traits of separations systems, and increase efficiency and selectivity. This requires a multimodal approach, yielding a molecular-level understanding of competitive intermolecular interactions. These interactions may be responsible for emergent behavior, such as solution order from the molecular to macroscopic scales, and coupled dynamic behavior across timescales (including metastability).

New methodology

The development of new characterization measurements, including upgrades to US Department of Energy national user facilities, have begun to reveal complex solution structures in the organic phase and the organization at the liquid-liquid interface that presumably influences mass transfer mechanisms. For example, the high coherent flux enabled by upgrades to the Advanced Photon Source has facilitated significant advances to coherent imaging techniques, including fast self-assembly processes that are relevant to the aggregation phenomena associated with non-ideal LLE. Essential to experimental interpretation and the development of predictive capability are advances to physics-based atomistic modeling and data analysis, an area we entered during the late 2000s. At that time, density functional theory was a mainstay to predict geometric and electronic properties of actinides, yet the ability to sample the ensembles of different environments in the multicomponent solutions of LLE was still in its infancy. These limitations have been largely overcome within the last decade as major investments in classical force field development, alongside advances in ab-initio molecular dynamics methods, now support simulations of multicomponent actinide-containing solutions and their interfaces. Importantly, when more realistic simulations are performed, the analysis of the data becomes critical because complex correlations emerge that are challenging to identify a priori. In the same vein, our laboratory has leveraged techniques from data science and adapted applied mathematics methods to elucidate a hierarchical, multiscale understanding of actinide LLE. These methods can be classified into two major groups, using either:

- Graph theoretical methods, or network analysis, of intermolecular interactions, including pattern recognition from spectral graph theory, clustering, and community analyses
- Geometric topology methods to characterize liquid/liquid interfaces

We have worked over the last decade to elucidate the complex speciation of actinides in the aqueous phase, how they traverse the phase boundary, and studied their behavior in highly non-ideal organic phases that exhibit aggregation phenomena. Here, we briefly discuss the interfacial chemistry in actinide LLE and how the fusion of data science and applied mathematics with modeling and simulation is leading to new strategies for optimizing separations efficiency.

Using Google's algorithm to probe phase boundary processes

Consider an aqueous nitric acid solution containing UO_2^{2+} (uranyl ion), for which ab-initio and classical molecular dynamics methods predict the predominant species to be $UO_2(NO_3)^+ \cdot nH_2O$ in the bulk aqueous solution. Yet as the solution approaches the organic phase boundary, significant NO_3^- (nitrate ion) concentration gradients emerge which shift the equilibrium distribution of uranyl nitrate species to include more dinitrate complexes. In our laboratory, we map the changes to speciation and solvation environments by creating networks of all of the interactions of the ions with each other and water, and subsequently apply pattern recognition

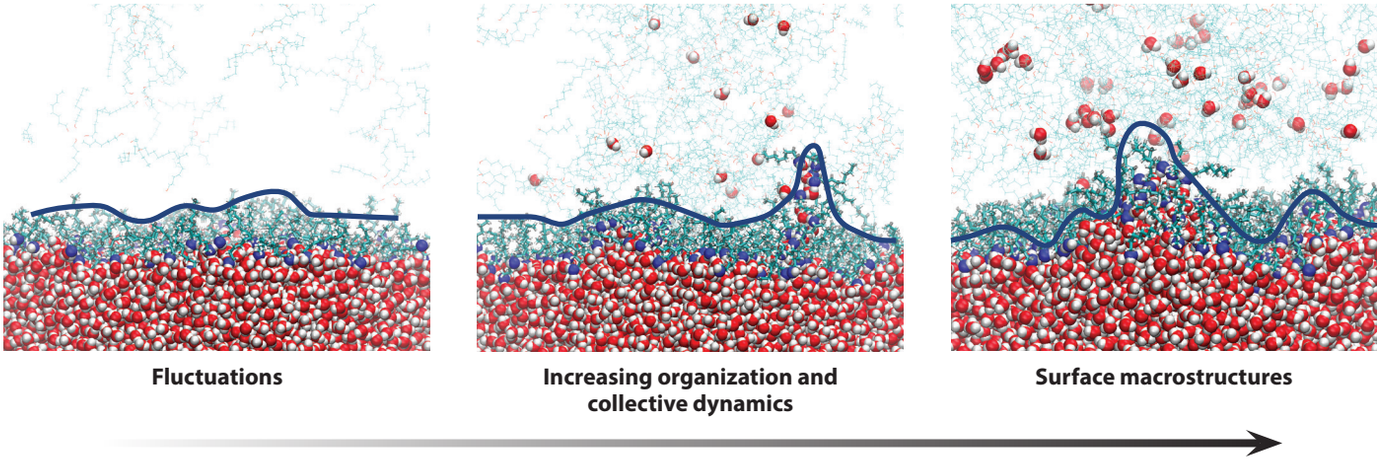

Figure 2. How the structure of the liquid/liquid interface changes under different conditions, from surface fluctuations that cause roughness on the left through capillary wave character to protrusions that cause transport on the right.

algorithms. One of the most successful approaches has been a modification of the PageRank algorithm, initially employed by Google to rank the importance of websites with user-specified search criterion. Using the patterns of intermolecular interactions, new software has been developed that inputs molecular simulation data and returns the set of all environments and compositions for the actinide and other solutes in solution.

By analyzing the ion environments as they approach the interface, we can also observe where they are likely to reside before transport. These data indicate that there are thermodynamic implications that derive from the heterogeneity of the oil/water interface. Although idealized pictures portray this interface as a flat surface, there are in fact local thermal oscillations overlaid on top of longer-range capillary wave fluctuations. These waves bridge the interface in such a way that their troughs penetrate the aqueous phase and the crests correspondingly peak in the organic phase. Accounting for this behavior, simulations predict that ions which sit at the aqueous troughs of the wave fronts keep more of their waters of solvation (which is favorable) than ions that migrate into the organic crest region (unfavorable). Importantly, surface-active ligands are predicted to modulate the surface heterogeneity—when a more "flat" or interdigitated surface is formed, the energetic penalties associated with solvation loss are removed so as to increase the number of ions in the interface. If transport across the interface is a rate-limiting process, an increase in actinide ion concentration has the potential to drive the transport process forward.

Our understanding of the specific solute transport mechanism also relies heavily upon interfacial heterogeneity—in which surface crests and troughs can support the formation of surface structures that help disengage solutes from the interface so that they can migrate into the organic phase. Tributyl phosphate (TBP), employed in the PUREX process, has been shown to amplify the crests by forming water-bridged TBP dimers that disrupt solute/water hydrogen bond interactions and cause the formation of protrusions that transport a solute from the aqueous phase. Protrusions come in a myriad of shapes and sizes and can include solute species that are not observed in the organic phase. In the simplest example of TBP extracting water, many metastable TBP-water clusters are observed on the organic side of the interface, while the equilibrium structure in the bulk organic system is only the $TBP_2(H_2O)$ species. In order to understand the role of interfacial surface structures in transport mechanisms, we can again turn to data science and applied mathematics methods—adapting these techniques allows us to gain more chemical insights from simulation data.

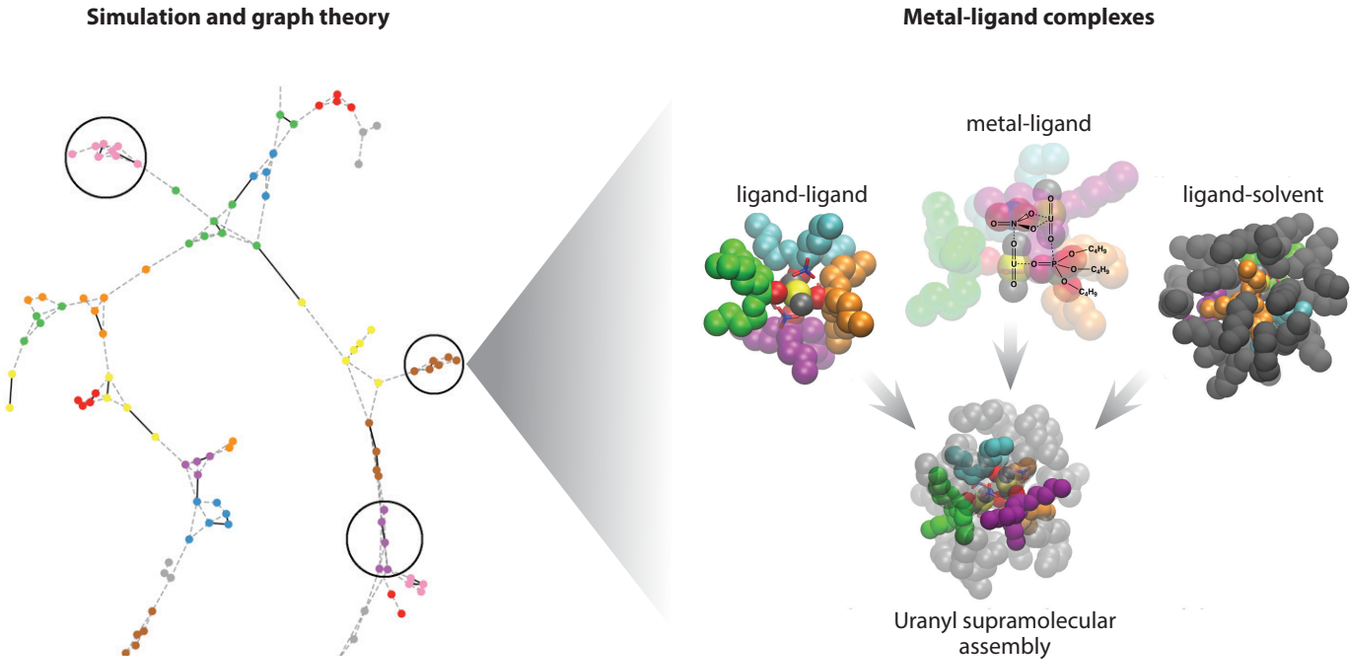

Figure 3. The aggregation of uranyl complexes causes longer-range organization, in which a collection of aggregates form networks and a dense phase that separates during third phase formation.

Molecular structures at the interface and in the organic phase

We have recently modified a method from image denoising, the Flat Norm algorithm, to identify the surface structures on soft matter. In essence, this algorithm works by systematically removing volumes on the surface, with precise labelling and tracking, until it is flat. We are applying this algorithm to identify all structures on the liquid/liquid interface and track them in time as solutes are transported. The aim is to correlate how surface-active ligands modulate interfacial organization and create surface structures that may have specific shapes or compositions that enable solute transport. By identifying the structural features of extracting ligands that facilitate protrusion formation, along with conditions that increase the ion concentration at the surface, we can optimize solution conditions that balance the selectivity of an extracting ligand for a specific actinide ion and its impact upon interfacial structure, with its ability to transport actinides across the surface.

A number of complex processes can occur once an actinide complex is in the organic phase. Self-assembly is emerging as an important non-ideal phenomena of actinide metal-ligand complexes under high metal-loading. X-ray scattering techniques, in combination with modeling and simulation, have indicated a wide range of aggregated species and there remains significant controversy regarding the role their structure, composition, and aggregation plays in extraction kinetics and efficiency. At the heart of interpreting the experimental scattering data are assumptions that are often made regarding the shape of aggregated species, in which spherical structures that would form from reverse micellular assemblies are often employed to fit the data. Yet molecular dynamics simulations combined with ab-initio modeling are revealing a much broader diversity of structural motifs that are equally capable of fitting experimental data and are based upon much more accurate physics describing the inter- and intramolecular interactions. A growing body of work from our laboratory and others is illustrating the importance of these molecular aggregates and how they may be sensitive to the specific coordination and solvation environments surrounding the metal ions of interest. Community and clustering

analysis techniques taken from the field of data science can identify the ensemble of aggregated species, and furthermore, can examine the interactions these species have with each other and how they impact phase phenomena. Using these methods, the diyl motif of actinyl complexes has been shown to lead to filamentous networks of aggregated species because the asymmetry induced by the diyl motif causes orientational preferences of the aggregate-aggregate interactions. This is in contrast to spherical ion-based aggregates that appear to lead to more isotropic interactions. The impact of such changes to long-range solution structure is still unclear, however they may provide additional design principles to control phase separation behavior under industrially-relevant metal loading conditions.

Summary

Development of actinide separations has largely relied upon idealized models of speciation in the aqueous and organic phases, as well as simplified concepts of transport across the liquid/liquid phase boundary. Advances to the modeling and simulation of actinide-containing solutions provides a window into the molecular processes that underpin actinide liquid/liquid extraction and includes the essential physics to predict non-ideal behavior. Non-ideality derives from complex-correlating relationships at the molecular level and across length and timescales. New data science methods are being used to elucidate the full spectrum of local environments surrounding actinide ions and their complexes based on network analysis of intermolecular interactions. The complex hierarchical structures at interfaces responsible for solute transport are being revealed using image-denoising technologies which have their roots in applied mathematics. In combination, next generation LLE methods will leverage these new relationships to optimize mass transfer efficiency and create robustness.

Further reading:

1. *A Research Agenda for Transforming Separation Science, National Academies of Sciences, Engineering, and Medicine, 2019, The National Academies Press, DOI:10.17226/25421*
2. *https://www.aps.anl.gov/files/APS-Uploads/Aps-Upgrade/Beamlines/APS-U%20Early-Science-103015-FINAL.pdf*
3. *P. Rao, Z. Kolarik, "A Review of Third Phase Formation in Extraction of Actinides by Neutral Organophosphorus Extractants Solvent," Extr. Ion Exch., 1996, 14, 955–993.*
4. *M.J. Servis, E. Martinez-Baez, A.E. Clark, "Hierarchical Phenomena in Multicomponent Liquids: Methods, Analysis, Chemistry," Phys. Chem. Chem. Phys., 2020, 22, 9850.*
5. *E. Alvarado, Z. Liu, M.J. Servis, B. Krishnamoorthy, A.E. Clark, "A Geometric Measure Theory Approach to Identify Complex Structural Features on Soft Matter Surfaces," J. Chem. Theory Comput., 2020, ASAP, DOI: 10.1021/acs.jctc.0c00260.*

Modeling Point Defects and Fission Gas Diffusion in Nuclear Fuels

David Andersson, Christopher Matthews, Michael Cooper, Romain Perriot, Chris Stanek
Los Alamos National Laboratory, P.O. Box 1663, Los Alamos, New Mexico

Nuclear fuel generates heat in reactors via fission which is transformed into electricity by generators driven by steam turbines. The use of uranium for nuclear fuels is by far the single largest use of actinides in our society. Given the reliance on uranium and its compounds, the use of nuclear fuels is fundamentally underpinned by actinide science. For example, the complex phase diagrams of uranium compounds, the propensity of multiple oxidation states, and the intricate magnetic properties are all known to influence various aspects of nuclear fuel performance.

Light water reactors (LWRs) are the dominant reactor type for electricity production globally, with uranium dioxide (UO_2) as the preferred fuel. LWRs have been very successful and provide approximately 20% of the electricity in the United States. By optimizing the UO_2 fuel and zirconium cladding encasing the fuel pellets in long rods, the nuclear industry has achieved a capacity factor (percentage of time the reactor produces electricity) close to 95%, increased output via power uprates (maximum power produced by a plant), and extended the discharge burnup (energy extracted over the lifetime of the fuel), all of which are examples of fuel development impacting economic drivers. Although severe accidents are extremely rare, a few instances have shaped the nuclear industry, most recently the incident at the Japanese Fukushima Nuclear Power Plant in 2011. As a response to this event, the Department of Energy initiated development of several accident tolerant fuel (ATF) concepts in close partnership with nuclear fuel vendors. Motivated by both ATFs and economic drivers, advanced fuel performance simulation capabilities have co-evolved to evaluate fuel behavior during both normal reactor operation and accident scenarios, with the ultimate goal of assessing the margin to fuel failure.

At the engineering or fuel pellet scale, these simulations rely on the finite element method (a widely used method for solving problems in mathematical models) as implemented in the BISON fuel performance code, for example. Fuel performance simulation tools rely on accurate models for material properties under irradiation, without which the simulations cannot be successful. Models for new fuel materials are costly and time-consuming to develop, in large part due to the need for extensive irradiation tests. Advanced multi-scale modeling and simulation methods are being used to support traditional empirical (e.g., experimentally driven) model development, with the additional goal of improving fidelity by tying the models closer to the physical mechanisms controlling fuel performance.

Multi-scale simulations of point defects and gas diffusion in UO_2

The rare gas atoms krypton and xenon are produced as fission products during the burnup of reactor fuels. Xenon (Xe) is the dominant fission gas and often used in simulations to represent the aggregate fission gas behavior. These gas atoms form bubbles both within the grains and on grain boundaries, which results in swelling

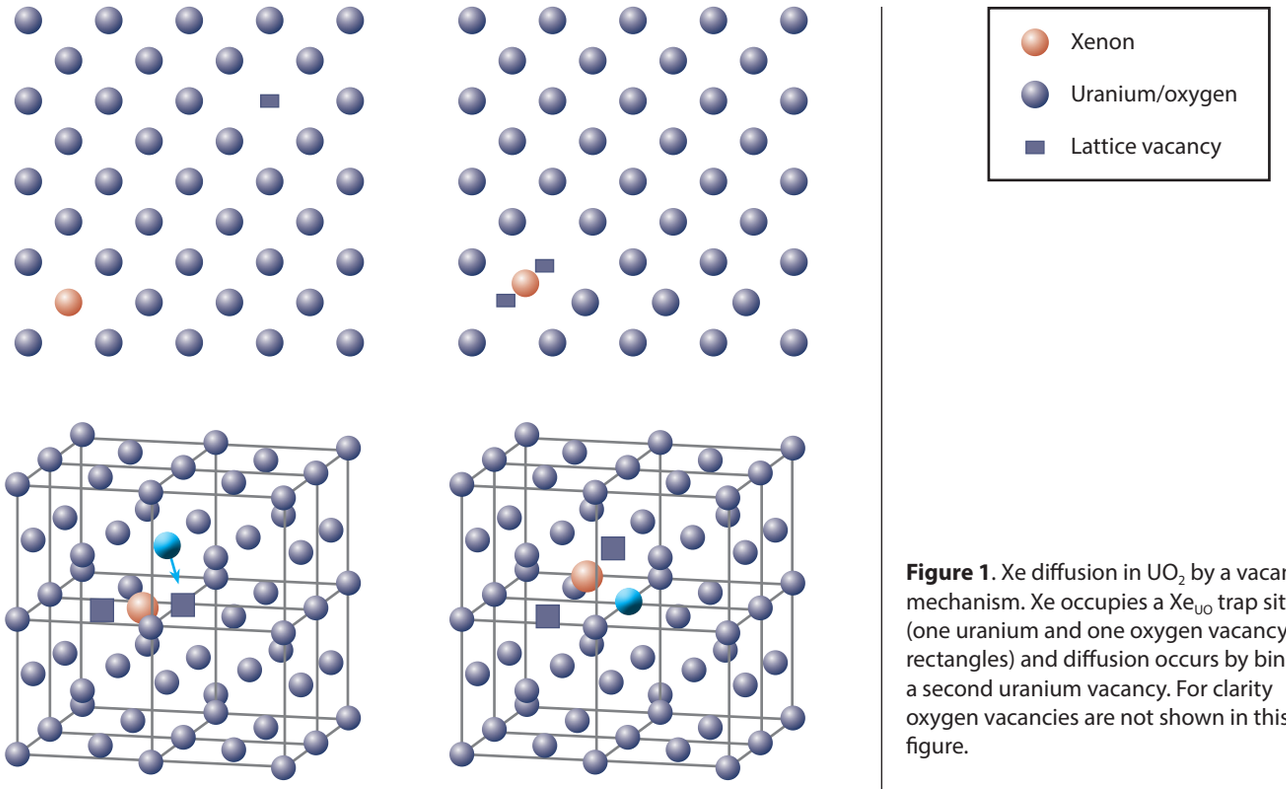

Figure 1. Xe diffusion in UO_2 by a vacancy mechanism. Xe occupies a Xe_{UO} trap site (one uranium and one oxygen vacancy, rectangles) and diffusion occurs by binding a second uranium vacancy. For clarity oxygen vacancies are not shown in this figure.

severely affecting the mechanical properties of the fuel. The gas is released from the grain boundaries after reaching a critical concentration. Point defects are defined as locations where an atom is missing or is in an irregular place in the lattice structure. They can be formed by thermal mechanisms or radiation damage, and impact many processes important for fuel performance through their connection to diffusion, such as fission gas retention/release, swelling, and creep. Point defects include self-interstitial atoms, interstitial impurity atoms, substitutional atoms, and vacancies.

Examples of the multi-scale simulation approach include the application of atomic-scale simulation methods to predict fundamental properties of point defects in UO_2, doped UO_2, and U_3Si_2, and using thermodynamic and kinetic models captured in cluster dynamics simulations to predict diffusion properties. Atomistic simulations involve both density functional theory (DFT) calculations, which are capable of resolving the often-complex properties caused by the uranium 5f electrons, and more computationally-efficient empirical potentials to describe the forces between atoms.

The link between fundamental point defect properties obtained from atomic scale simulations and the complex performance properties in irradiated fuels is established by using longer length and timescale simulation methods. In the present case, this involves thermodynamic and kinetic models implemented in a cluster dynamics simulation framework. The role of the cluster dynamics method is to keep track of point defect and fission gas evolution, including non-stoichiometry prevalent in many actinide compounds.

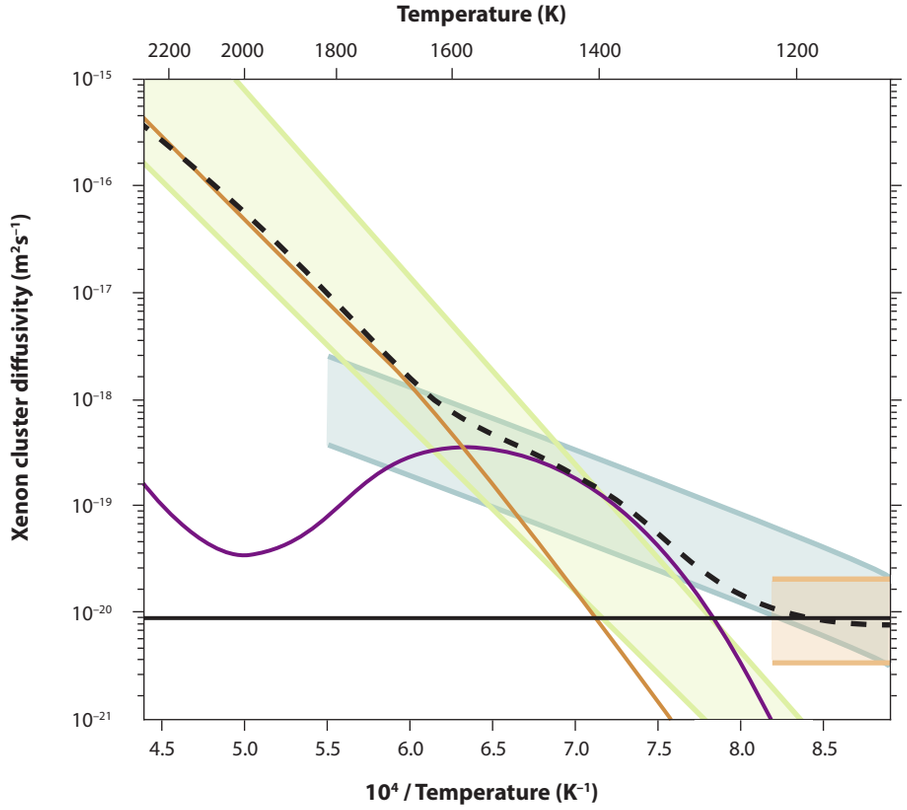

Figure 2. The predicted Xe diffusion coefficient in UO_2. This Arrhenius plot tells us the diffusion rate of Xe as function of temperature (note the temperature decreases from left to right) in the fuel under irradiation. This governs the time it takes for Xe to reach bubbles and grain boundaries, and to be released from the fuel. The highlighted fields indicate the range of experimental data and also the high (T > 1600 K), intermediate (1200 < T < 1600 K), and low (T < 1200 K) temperature regimes with distinct Arrhenius slopes corresponding to different diffusion mechanisms. The contribution from the Xe_{U2O} and Xe_{U4O3} clusters are highlighted by separate curves. The total diffusivity agrees well with experimental data.

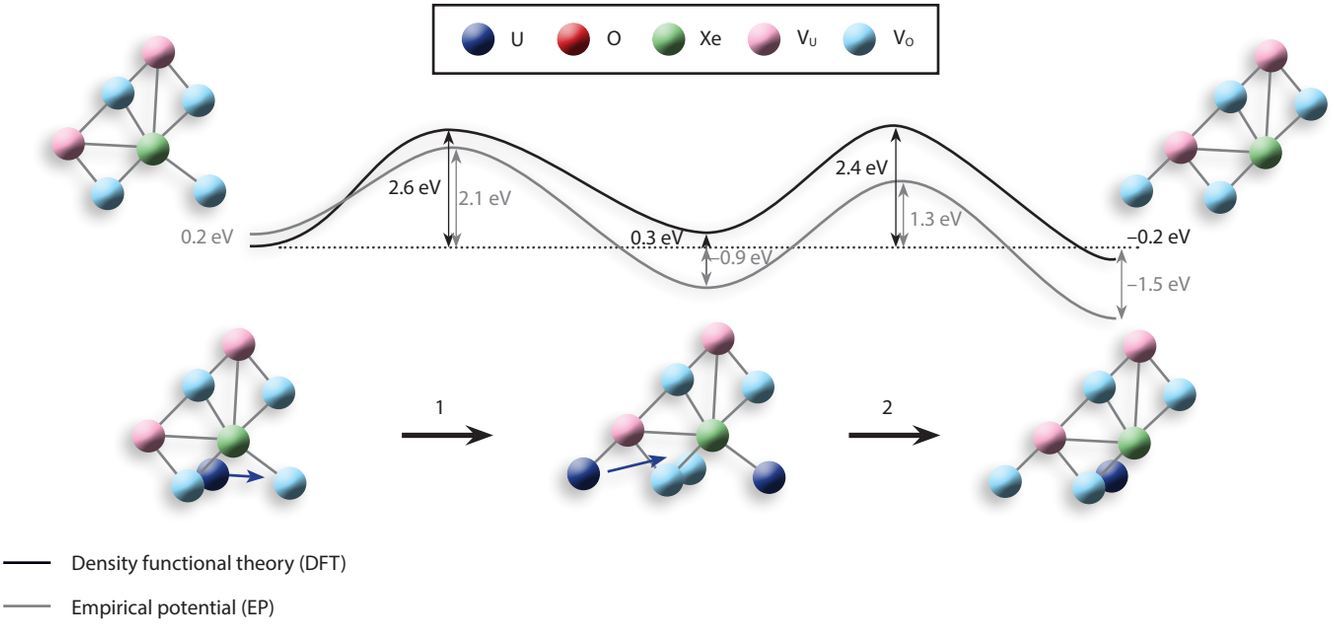

Figure 3. The diffusion mechanism for the XeU_4O_3 cluster (Xe in a cluster composed of four uranium and three oxygen vacancies), which is responsible for irradiation-enhanced diffusion in UO_2 at intermediate temperatures, see Figure 2.

Diffusion of gas atoms in UO_2 occurs by vacancy mechanisms. In almost-stoichiometric $UO_{2\pm x}$ ($x < 0.001$) under thermal equilibrium conditions (no irradiation), Xe atoms occupy a trap site consisting of both a uranium and oxygen vacancy. Diffusion takes place by binding a second uranium vacancy and moving the cluster center of mass by a concerted mechanism (Fig. 1). By using DFT to calculate point defect formation energies, cluster binding energies, migration barriers, and empirical potentials for the corresponding entropies, the important fission gas diffusion coefficient may be predicted (Fig. 2). Successful prediction of diffusion coefficients at a quantitative level is only possible by accounting for the complexities of UO_2, specifically the strongly-correlated U 5f electrons, the resulting non-stoichiometry in $UO_{2\pm x}$, the charge state of defects (distribution of electrons and holes) and the temperature dependence of the oxygen potential due to oxygen buffering. The fission gas diffusion coefficient governs the time it takes to move gas atoms from the grain interior to grain boundaries, where continuous gas accumulation eventually leads to the growth of large gas bubbles that form interconnected paths, ultimately releasing gas from the fuel pellet. The fission gas diffusion rate discussed above is only valid at very high temperatures ($T > 1600$ K) in a reactor, where irradiation-induced point defects are quickly annealed to their thermodynamic equilibrium values.

Irradiation effects

In order to predict the point defect behavior at intermediate temperatures ($1200 < T < 1600$ K) under irradiation, the creation, annihilation, and interaction of point defects and Xe atoms must be considered using a model that does not assume thermal equilibrium. In the field of nuclear materials such driven systems are often modeled using cluster dynamics methods. These record a large number of clusters composed of point defects, and how they interact with each other and microstructure sinks, e.g., grain boundaries and voids, using a set of coupled ordinary differential equations (ODEs). By using this type of model with parameters for UO_2 obtained from DFT and empirical potential atomistic calculations, it is possible to show that the concentration of extended Xe-vacancy clusters increases below approximately 1600 K. Some of the extended clusters are also able to migrate with a low barrier (Fig. 3). Altogether, this results in the Xe_{U4O3} cluster (Xe in a cluster composed of four uranium and three oxygen vacancies) starting to contribute to diffusion at around

1600 K under irradiation. This explains the experimentally observed kink in the Arrhenius plot of the diffusion coefficient under irradiation around that temperature, see Fig. 2. This result is intriguing and it is worth noting that identifying the cluster responsible for the change in slope would have been virtually impossible without the help of atomic scale and cluster dynamics simulations.

At low temperatures (T < 1200 K), the lattice disorder directly introduced by the irradiation damage through so-called thermal spikes is the main contributor to diffusion, which leads to an athermal contribution to the diffusivity (Fig. 2). This behavior has been reproduced in molecular dynamics simulations and constitutes the final part in establishing a mechanistic model for fission gas diffusion in UO_2 across the full temperature and irradiation range of interest to reactor applications. The mechanistic diffusion model may be represented as the summation of two Arrhenius functions and term independent of temperature, which makes it easy and computationally efficient to use in engineering-scale fuel performance simulations.

Extending the model to doped UO_2 and U_3Si_2

The biggest value of the multi-scale simulation approach is not to reproduce known data and empirical models for UO_2, but rather to apply it to new fuels (such as U_3Si_2) or new fuel compositions (e.g., doped UO_2). The model originally derived for UO_2 may be modified by accounting for changes in the thermochemistry introduced by a dopant such as Cr_2O_3. The change in oxygen potential affects the concentration of point defects, which translates into shifts in the relative concentration of Xe-vacancy clusters. By implementing the changes in thermochemistry, the cluster dynamics model is able to resolve the changes in cluster concentrations and the impact on diffusivity. An increase in Xe diffusion is predicted for all temperatures, although the mechanism is different at high and low temperatures. At high temperatures, the increase is driven by higher concentrations of uranium vacancies (compared to UO_2) due to the more oxidizing conditions created by Cr_2O_3 above approximately 1800 K. At intermediate temperatures, the more reducing conditions increase the concentration of oxygen vacancies, and thus the relative importance of the most mobile extended Xe-vacancy cluster. Note that the uranium vacancies themselves are created by irradiation in the intermediate-temperature regime and are mostly decoupled from the equilibrium thermochemistry, which explains why the decreased concentration of thermal equilibrium uranium vacancies under reducing conditions is not important for the predicted irradiation-induced diffusivity. The fission gas diffusion model for doped UO_2 has been successfully transferred to fuel performance simulations.

Although doped UO_2 differs from pure UO_2, many properties are only marginally modified because the doping levels are of the order 0.1 atom-percent. Modeling a completely new fuel presents a much more significant challenge. Nevertheless, the framework developed and validated for UO_2 can be extended to U_3Si_2, for example, which has been proposed as a new fuel for LWRs. The main benefit of this fuel is the higher uranium density and increased thermal conductivity, due to it being metallic rather than insulating or semi-conducting like UO_2.

In order to study fission gas behavior in U_3Si_2, the DFT methodology had to be refined to avoid lattice instabilities for the experimentally observed crystal structure. In particular, the treatment of U 5f electrons had to include terms to account for strong correlations, which is similar to UO_2 where the same treatment is required to capture its semi-conducting character. The calculation of point defect properties and their connection to fission gas diffusion then follows a similar path as for UO_2.

However, the problem is slightly more complicated because the U_3Si_2 crystal structure is tetragonal rather than cubic, which leads to anisotropic diffusion (i.e., asymmetrical in space), therefore mechanisms have to be investigated for all crystallographic directions. Additionally, both the U and Si lattice sites participate in gas diffusion, while for UO_2 the physics is strongly dominated by U vacancies as oxygen diffusion is sufficiently rapid to not impact the rate-controlling migration steps. The results for U_3Si_2 will not be described in any detail, however the approach used for UO_2 was successfully transferred to U_3Si_2 and the resulting diffusion model was implemented in the BISON fuel performance code by collaborators at Idaho National Laboratory to predict gas release and swelling in the first irradiation tests recently performed.

Summary

The application of atomic-to-continuum simulation techniques to point defects and fission gas diffusion in nuclear fuels has demonstrated the value of the multi-scale approach. This success emphasizes how it can be combined with experiments to extend our knowledge of critical processes in nuclear fuels and generate additional data points for fuel performance assessments. It is important to stress that the approach described here relies on modeling and simulations working in tandem with experiments to facilitate progress at a rate that is faster than any one of them applied separately. This approach will be important for the development of new nuclear fuels and relies heavily on progress in actinide science, specifically atomic scale modeling of uranium compounds and their chemistry.

Further reading:

1. *D.A. Andersson, X.-Y. Liu, B. Beeler, S.C. Middleburgh, A. Claisse, C.R. Stanek, "Density Functional Theory Calculations of Self- and Xe Diffusion in U_3Si_2," J. Nucl. Mater., 2019, 515, 312.*
2. *M.J. Noordhoek, D. Andersson, A. Chernatynskiy, S. Middleburgh, T.M. Besmann, "Phase Equilibria in the U-Si System from First-Principles Calculations," J. Nucl. Mater., 2016, 479, 216.*
3. *R. Perriot, C. Matthews, M. Cooper, B.P. Uberuaga, C.R. Stanek, D.A. Andersson, "Atomistic Modeling of Out-of-Pile Xenon Diffusion by Vacancy Clusters in UO_2," J. Nucl. Mater., 2019, 520, 96.*
4. *C. Matthews, R. Perriot, M.W.D. Cooper, C.R. Stanek, D.A. Andersson, "Cluster Dynamics Simulation of Uranium Self-Diffusion During Irradiation in UO_2," J. Nucl. Mater., 2019, 527, 151787.*
5. *M.W.D. Cooper, C.R. Stanek, J.A. Turnbull, B.P. Uberuaga, D.A. Andersson, "Simulation of Radiation Driven Fission Gas Diffusion in UO_2, ThO_2 and PuO_2," J. Nucl. Mater., 2016, 481, 125.*
6. *D.A. Andersson, P. Garcia, X.-Y. Liu, G. Pastore, M. Tonks, P. Millett, B. Dorado, D.R. Gaston, D. Andrs, R.L. Williamson, R.C. Martineau, B.P. Uberuaga, C.R. Stanek, "Atomistic Modeling of Intrinsic and Radiation-Enhanced Fission Gas (Xe) Diffusion in $UO_{2\pm x}$: Implications for Nuclear Fuel Performance Modelling," J. Nucl. Mater., 2014, 451, 225.*
7. *D.A. Andersson, B.P. Uberuaga, P.V. Nerikar, C. Unal, C.R. Stanek, "U and Xe Transport In $UO_{2\pm x}$: Density Functional Theory Calculations," Phys. Rev. B, 2011, 84, 054105.*
8. *R.L. Williamson, J.D. Hales, S.R. Novascone, M.R. Tonks, D.R. Gaston, C.J. Permann, D. Andrs, R.C. Martineau, "Multidimensional Multiphysics Simulation Of Nuclear Fuel Behavior," J. Nucl. Mater., 2012, 423, 149.*
9. *C. Matthews, R. Perriot, M.W.D. Cooper, C.R. Stanek, D.A. Andersson, "Cluster Dynamics Simulation of Xenon Diffusion During Irradiation in UO_2," J. Nucl. Mater. 2020; doi.org/10.1016/j.jnucmat.2020.152326.*

Magnetic Properties of f-Element Complexes

Wayne Lukens[1] with editorial additions by Owen Summerscales[2]
[1]Chemical Sciences Division, Lawrence Berkeley National Laboratory, Berkeley, California
[2]Los Alamos National Laboratory, Los Alamos, New Mexico

The unique magnetic properties of lanthanide and actinide ions make their compounds among the most useful magnetic materials. Lanthanide-based magnets, such as $Nd_2Fe_{14}B$, are the strongest permanent magnets available and are widely used in electric vehicle motors and wind turbine generators. In addition to their utility, the magnetic behavior of lanthanide and actinide compounds is both fascinating to study and challenging to model theoretically. The magnetic behavior of these ions is intimately related to their electronic structures—as a result, it is impossible to understand their magnetic behavior quantitatively without an equally detailed understanding of their electronic structures. Conversely, if the calculated magnetic behavior of an actinide ion matches experiment, the calculated electronic structure should be similar to the actual electronic structure of the system. In this article, the electronic structures and magnetic properties of isolated lanthanide and actinide complexes are briefly introduced. Some highlights of magnetic behavior among these ions are discussed including some open questions where theory is needed to resolve perplexing magnetic behavior.

A particularly useful theory for thinking about magnetic behavior of lanthanide and actinide complexes is crystal field theory (CFT). This is an empirical model of the electronic structure of metal ions that is parameterized using experimental observations, usually the energies of the excited states. While it can be quite accurate for lanthanide ions, its utility lies in its relative simplicity rather than accuracy. This simplicity allows one to understand how changes in the structure of a complex can affect magnetic properties. For this reason, the electronic structures of lanthanide and actinide ions will be described using a CFT framework. In the following we introduce the basic mathematical formulation of these electronic states which subsequently allows us to discuss the details of these compounds' magnetic properties.

Hamiltonian formulations

A Hamiltonian (H) is a mathematical function that describes the energy of a system in terms of kinetic and potential energy. The simplest CFT Hamiltonian is the summation of the Hamiltonians of the crystal field (H_{CF}), electron-repulsion (H_{ee}), and spin-orbit coupling (H_{SO}). In lanthanide and actinide ions, the largest term by far is electron repulsion, H_{ee}, with an energy scale of 10^4 cm^{-1}. The next largest contribution is spin-orbit coupling, H_{SO}, with an energy scale of 10^3 cm^{-1}. The smallest contribution to the Hamiltonian is the crystal field, H_{CF}, with an energy scale of 10^2 cm^{-1} for lanthanide ions and 10^3 cm^{-1} for actinide ions. Although H_{CF} is the smallest term in the CFT Hamiltonian, it is the most important for understanding the magnetic behavior of actinide and lanthanide complexes, especially the relaxation of single molecule magnets (SMMs). While the Hamiltonian for the crystal field, H_{CF}, is a complex mathematical equation, the role of crystal field parameters can be explained more simply, albeit using some fundamental quantum concepts.

These four quantum numbers are used to describe the probable location of an electron in an atom:

Number	Symbol	Possible values
Principal quantum number	n	1, 2, 3, 4...
Angular momentum quantum number	ℓ	0, 1, 2... (n–1)
Magnetic quantum number	m_ℓ	–ℓ,... –1, 0, +1, ... ℓ
Spin quantum number	m_s	+½, –½

We can describe an electron in an atom using four quantum numbers:

- **Principal quantum number (n)**. This designates the principal electron shell; for lanthanide f-electrons, $n = 4$, and for actinides, $n = 5$.
- **Orbital angular momentum quantum number (ℓ)**. This describes the shape/type of orbital; the f-orbitals have $\ell = 3$.
- **Magnetic quantum number (m_ℓ)**. This is the projection of angular momentum in space and depends on the orbital angular momentum quantum number ℓ. Given a certain value of ℓ, m_ℓ can have values ranging from $-\ell$ to $+\ell$, so it can be zero, a negative integer, or a positive integer.
- **Spin quantum number (m_s)**. An electron has $s = ½$. Each orbital contains no more than two electrons, whose spin must be opposed (m_s ±½), referring to "spin up" and "spin down" states.

These numbers describe an individual electron, but for the whole system (e.g., an atom or ion), we use the uppercase designation for orbital angular momentum and spin, L and S respectively.

Russell-Saunders coupling: A primer

Because H_{CF} is the smallest term for f-element complexes it is simpler to discuss the electronic structure in terms of states (the product of all electrons) rather than in terms of individual electrons as is done in transition metal chemistry. The states can be described using the sums of the orbital angular momentum ($L = \sum m_\ell$) and spin angular momentum ($S = \sum m_s$) of the f-electrons. The resulting states are defined by their total angular momenta, J, which has values from $|L–S|$ to $L+S$, representing the different combinations of momenta.

The state with a given value of J is split into sub-states described by the total angular momentum quantum number, m_J, which ranges from $-J$ to $+J$ in steps of one. This generates $(2J + 1)$ different values of m_J. These individual m_J states are usually described using a 'ket', $|m_J\rangle$, which is just a shorthand way of saying "the wavefunction for the electronic state with a total angular momentum quantum number of m_J."

The crystal field parameters further change the energies of these $|m_J\rangle$ states and allow them to interact with each other ('mix') to form new states that are a combination of the original states. Exactly how the states change in energy and mix with each other determines the magnetic properties of the ion, which is best explained using an example, Dy^{3+}.

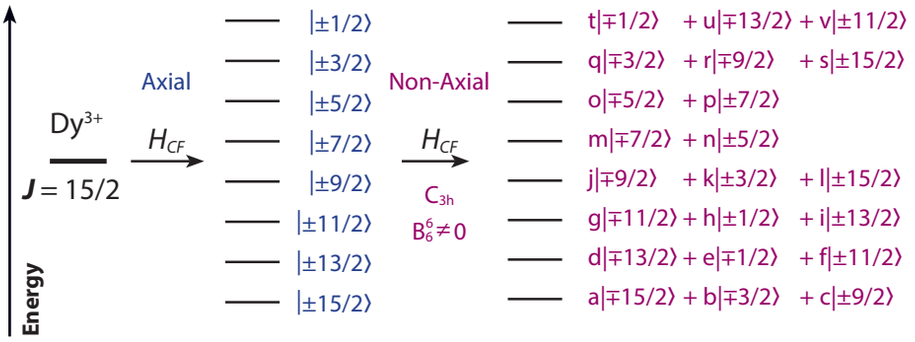

Figure 1. This figure illustrates how we determine the electronic m_J sub-states, and therefore the magnetic properties, for a Dy^{3+} complex with D_{3h} symmetry. Splitting of the $J = 15/2$ ground state of Dy^{3+} is caused by the crystal field parameters. The axial parameter changes the energies of $|m_J\rangle$ and the non-axial B_6^6 term mixes m_J states with states having m_J ±6 to produce the states on the right. The coefficients a–v are the contributions of the m_J states in the new states resulting from mixing by B_6^6.

The lanthanide ion Dy^{3+} has nine f-electrons, and the ground state has $J = 15/2$ and consists of 16 sub-states with $m_J = -15/2, -13/2, \ldots, 15/2$. The crystal field parameters describe the degree of splitting and mixing of the orbitals and how the energies of these $|m_J\rangle$ sub-states vary with respect to each other. To understand how this occurs, it helps to separate the crystal field parameter into two groups according to their symmetries: axial crystal field parameters, B_0^k, and non-axial parameters, B_q^k ($q \neq 0$; both k and q describe the symmetry of the parameter). The axial crystal field parameters represent the effects of ligand interactions (electrostatic charges and orbital overlap) along the z-axis of the molecule. The non-axial crystal field parameters represent the effects of ligand interactions along the x- and y-axes. The main effect of the non-axial parameters is to 'mix' together $|m_J\rangle$ states values of m_J that differ by q (the subscript in B_q^k), which has a profound effect on the magnetic properties of lanthanide and actinide complexes.

Most of the non-axial crystal field parameters are zero for high symmetry. For example, in D_{3h} symmetry, only B_6^6 is non-zero (D_{3h} is a term that describes the symmetry characteristics of the molecule; it is the symmetry of a trigonal prism). These effects of the axial and non-axial crystal field parameters are illustrated in Fig. 1. The magnitude of the crystal field parameters is largely due to orbital overlap, so the crystal field parameters of the actinides are much larger than those of the lanthanides due to the greater radial extent of the 5f-orbitals relative to the 4f-orbitals.

Single molecule magnets (SMMs)

The most significant recent experimental advance in f-element magnetism has been the development of lanthanide SMMs. An SMM is a complex that retains its magnetization in the absence of a magnetic field in analogy to a permanent magnet. Below the blocking temperature (T_B), SMMs display slow magnetic relaxation, therefore the higher the value of T_B, the greater utility of the magnet. The field began with the discovery of SMM behavior in a manganese cluster, $Mn_{12}O_{12}(OAc)_{16}(H_2O)_4$ ("Mn_{12}"), by Sessoli and coworkers, who also developed the theory of SMM behavior in a series of papers from 1993 to 1998. In the initial description, an SMM can be described using a double-well potential in which one well is spin up and the other is spin down (Fig. 2). Once the molecule has had its magnetic moment aligned by successive application and removal of a strong magnetic field, the molecule can only

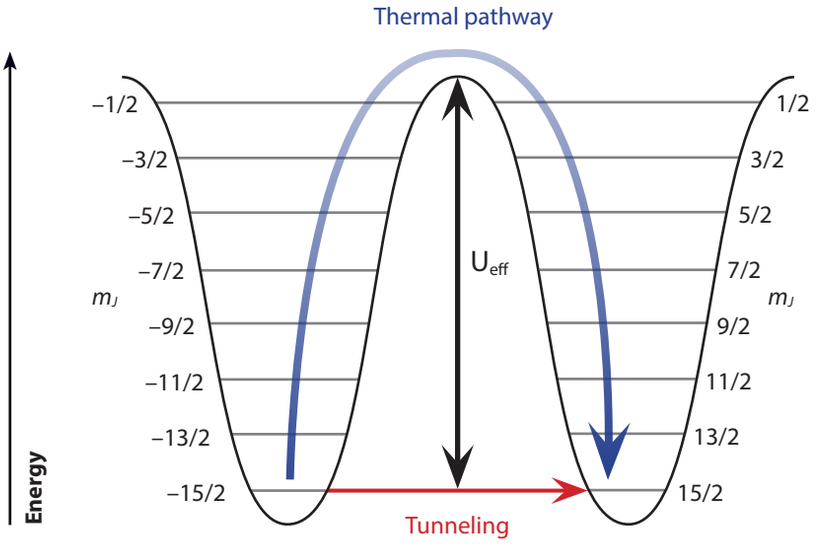

Figure 2. Magnetic relaxation pathways illustrated using a double-well potential for a hypothetical Dy^{3+} ion with a perfectly axial crystal field.

lose this state by undergoing an internal electronic process that crosses the barrier between the wells to relax to the other spin state. This may be done by crossing the barrier (U_{eff}) in a thermally-activated (Orbach) process, which is the ideal situation. However, the barrier can also be crossed by tunneling between the wells (quantum tunneling of magnetization, QTM) or by the familiar pathways involving spontaneous and stimulated emission of photons. Spontaneous and stimulated emission pathways are well-understood and generally minor pathways in these systems due to the very small energy differences between the states on either side of the well.

For the Mn_{12} cluster, T_B was measured as 3 K and U_{eff} was 42 cm^{-1}. While single molecule magnetism was discovered in transition metal clusters, the best SMMs reported to date are lanthanide complexes, some of which have values of $T_B > 80$ K and $U_{eff} > 1400$ cm^{-1} (a large crossing barrier, U_{eff}, is desirable for creating effective magnets). Lanthanide SMMs can also be described using a double-well potential, but for single lanthanide ions, the states are simply the crystal field states, $|m_J\rangle$ resulting from the splitting of the ground state. For Dy^{3+}, the double-well potential for a system with purely axial symmetry (all non-axial crystal field parameters are zero) is shown in Fig. 2.

Explaining effective lanthanide SMMs

A particularly notable dysprosium SMM is $Dy(C_5H_2{}^tBu_3)_2B(C_6F_5)_4$, abbreviated $Cp^{ttt}{}_2Dy^+$, which was reported independently in 2017 by Guo et al. and Goodwin et al. This complex was notable for its record-breaking values of T_B and U_{eff}, 53 K and ~1200 cm^{-1}, respectively. Even more impressive is the theoretical modeling of its thermally-activated relaxation pathways (Fig. 3b).

The primary reason for the high T_B and U_{eff} values is that the crystal field produced by the Cp^{ttt} ligands is almost perfectly axial (i.e., the non-axial crystal field parameters have small values) for the states with the largest values of m_J. In other words, the state labeled "$|\pm15/2\rangle$" consists almost entirely of $|\pm15/2\rangle$ with little contribution from other $|m_J\rangle$ states. In $Cp^{ttt}{}_2Dy^+$, this is true for the excited states up to and including $|\pm7/2\rangle$. The $|\pm5/2\rangle$, $|\pm3/2\rangle$, and $|\pm1/2\rangle$ states are all significantly mixed with each other, which has an important effect on the magnetic relaxation. First, the measured barrier to relaxation is approximately 1200 cm^{-1}, which is the energy of the $|\pm5/2\rangle$ state. More importantly, as shown by the calculated relaxation pathways (red arrows in Fig. 3b), the primary route for crossing the barrier involves tunneling

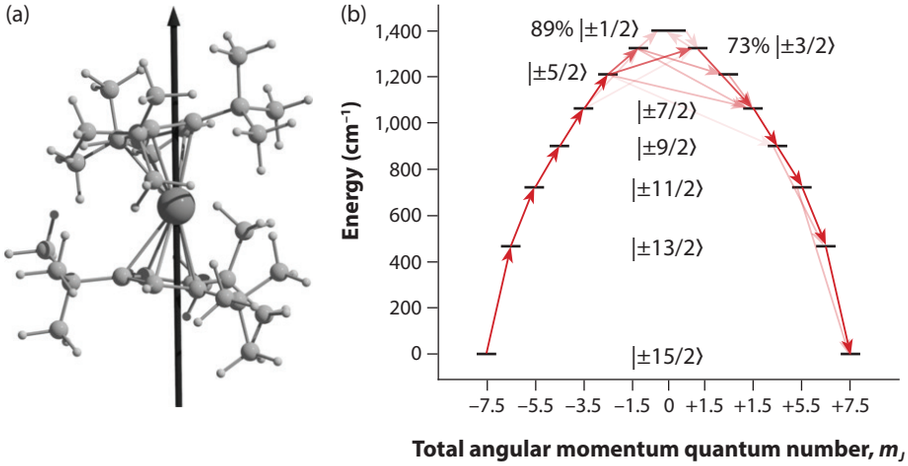

Figure 3. (a) Molecular structure of $Cp^{ttt}_2Dy^+$, taken from the article "A dysprosium metallocene single-molecule magnet functioning at the axial limit" by Guo and co-workers, published in Angewandte Chemie International Edition in 2017. (b) Molecular modeling results showing energies (horizontal lines) and relaxation pathways (red arrows where the intensity of the color is proportional to the importance of the pathway) for the electronic states of $Cp^{ttt}_2Dy^+$ resulting from the splitting of the ground state $^6H_{15/2}$ term (J = 15/2) by the crystal field of the two Cp^{ttt} ligands. The "hill" represents the barrier between the two wells illustrated in Fig. 2. Adapted from "Molecular magnetic hysteresis at 60 kelvin in dysprosocenium" published in Nature by Goodwin and co-workers in 2017.

through via the $|\pm5/2\rangle$ and $|\pm3/2\rangle$ states. Therefore, the calculated barrier to relaxation is approximately 1200 cm^{-1}, which is in remarkable agreement with experiment, rather than the total splitting of the J = 15/2 state of approximately 1400 cm^{-1}.

Mixing of magnetic states

The role that mixing of the $|m_J\rangle$ states plays in tunneling through the barrier has been explored by Fort, Lunghi, Escalera-Moreno, and their coworkers in addition to the authors of the $Cp^{ttt}_2Dy^+$ studies. Briefly, mixing of the $|m_J\rangle$ states by the non-axial crystal field parameters provides a facile pathway for the magnetization to relax by tunneling through the barrier due to coupling to the vibrational modes of the complex. The greater the mixing between a pair of states on either side of the barrier, the more likely the system is to tunnel through the barrier as a result of this coupling to a vibrational mode.

In $Cp^{ttt}_2Dy^+$, these pathways were modeled theoretically and are illustrated by red arrows in Fig. 3b. In addition, the authors determined which molecular vibrations were most responsible for the tunneling pathway: stretching modes involving the cyclopentadienyl C–H bonds. This information was used to construct new dysprocenium complexes with even higher values of T_B and U_{eff} by replacing all C–H bonds on the cyclopentadienyl ligands by C–alkyl bonds as illustrated by the work of Guo et al. in 2018.

The combination of experiment and computation highlighted by the work on $Cp^{ttt}_2Dy^+$, in addition to that of Fort, Lunghi, Escalera-Moreno, and others, explains how the vibrational modes allow SMMs to relax by tunneling through the thermal barrier. As shown by Liu et al., the same factors allow relaxation by tunneling in the ground state (QTM); furthermore, relaxation by this pathway can be mitigated by judicious choice of molecular symmetry (which is easier said than done!). However,

QTM is not solely due to this pathway. A number of other pathways for relaxation, especially coupling of the magnetization to other varying fields in the molecule, such those due to nuclear spins, may be responsible for QTM. What is currently unknown is how the properties of a given molecule can prevent or enhance relaxation by these routes. Further computational work would greatly help to understand the origins of QTM in the ground state.

Why so few actinide SMMs?

Despite the explosion of lanthanide SMMs, few actinide complexes display single molecule magnetism. Because the 5f-orbitals have greater radial extent than the 4f-orbitals, the crystal field parameters for actinide complexes are significantly larger than for their lanthanide congeners. For this reason, it was initially hoped that the larger axial crystal field parameters for the actinides would result in larger thermal barriers, U_{eff}, and SMMs with higher blocking temperatures. This has not been observed. The underlying reasons have been explored in detail by Escalera-Moreno, et al. The primary factor is that the greater radial extent of the 5f orbitals greatly increases the magnitudes of the non-axial crystal field parameters in addition to the axial ones. As discussed above, the non-axial parameters mix the $|m_J\rangle$ states, which creates facile tunneling pathways via coupling to molecular vibrations. This is even the case for $Cp^{ttt}_2U^+$, which is the uranium analog of $Cp^{ttt}_2Dy^+$.

Magnetism of actinide dioxides

This article is primarily concerned with molecular species, rather than bulk solids, due to the complexity introduced by interactions among neighboring spins in extended solids. However, two of the actinide dioxides, PuO_2 and CmO_2, are expected to have singlet ground states without the complication of interatomic spin coupling. Moreover, actinide dioxides have a simple cubic local structure, which makes them attractive both experimentally and computationally. The magnetism of PuO_2 illustrates where theory has reconciled experimental results that seem contradictory on first inspection, whereas CmO_2 magnetism is an example in which experimental results are not currently understood.

PuO_2 magnetism explained

The magnetic susceptibility of PuO_2 was measured in 1968 by Raphael and Lallement. Remarkably, PuO_2 displays temperature-independent paramagnetism (TIP) to 1000 K. This behavior was initially explained using CFT. The cubic crystal field created by the oxygen atoms in PuO_2 removes the degeneracy of the $J = 4$ ground state creating two triplet states (T_1 and T_2), a doublet state (E), and a singlet state (A_1). Experimentally, the ground state is A_1, and the presence of TIP to 1000 K suggests that no excited states are significantly occupied at this temperature. The magnitude of TIP allowed Raphael and Lallement to estimate that the T_1 state should be 2300 cm^{-1} above the ground state, which also explained why this excited state was not being thermally populated at 1000 K (1000 K is the energy equivalent of 695 cm^{-1}). In 1999, Kern et al. studied PuO_2 by neutron scattering, confirming the A_1 ground state, but finding that T_1 was only 990 cm^{-1} above the ground state. This much lower energy means that the T_1 state becomes significantly thermally populated above ~350 K, which apparently contradicts the observation that the magnetic susceptibility of PuO_2 is unchanging to 1000 K. In addition, the lower energy means that the theoretical magnetic moment is much greater than what is observed. Both experimental results, i.e., the TIP to 1000 K and that T_1 is 990 cm^{-1} above the ground state, are valid yet appear to be incompatible. This apparent contradiction has been explained by theory.

Despite its simple physical structure, calculation of the electronic structure of PuO_2 has proven extremely difficult because three electronic structures are close in energy: non-magnetic (the experimental result), antiferromagnetic, and ferromagnetic. As shown by Jomard et al., the most widely used density functional theory (DFT) approaches calculate that PuO_2 is either ferromagnetic or antiferromagnetic. The same holds true for hybrid DFT models as reported by Wen et al. However, other implementations of DFT produce the correct ground state: Colarieti-Tosti et al. included crystal-field splitting of the f-orbitals and reproduced both the non-magnetic ground state and the T_1 excited state energy. Shick et al. meanwhile used an Anderson impurity model to account for covalent interactions between Pu and O atoms, which accurately reproduced the non-magnetic ground state and T_1 energy. In addition, this model explained the lack of temperature dependence in the magnetic susceptibility. The calculated magnetic susceptibility was however significantly greater than experiment. Finally, Gendron et al. took a different approach using the complete active space self-consistent field (CASSCF) method and an embedded PuO_8^{12-} cluster. Their results reproduced the non-magnetic ground state, the T_1 state energy, and the lack of temperature dependence of the magnetic susceptibility. In addition, they reproduced the experimental value of the magnetic susceptibility, which is smaller than predicted largely due to mixing of excited state terms into the ground state by spin-orbit coupling (intermediate coupling).

CmO_2 magnetism still a mystery

Unlike for PuO_2, in which apparently contradictory experimental results were reconciled and explained by theory, the magnetic behavior of CmO_2 remains a mystery. The ground state term for CmO_2 has $J = 0$, which makes it a singlet state. Consequently, one would expect that the magnetic susceptibility would be temperature independent, which is observed in isoelectronic Am^{3+} complexes. However, as shown by Morss et al., the magnetic susceptibility of CmO_2 is temperature dependent with a large magnetic moment, which is not consistent with the suggested singlet ground state. As shown by Solderholm, temperature-dependent magnetism is a general property of Cm^{4+} complexes.

A number of hypotheses have been advanced to explain the temperature-dependent magnetic susceptibility in CmO_2. Experimentally, the presence of Cm^{3+} due to either imperfect stoichiometry or radiation damage can partially account for the observations. However, Solderholm showed that these explanations cannot readily account for the magnetic behavior of other curium compounds, in particular CmF_4. Likewise, a number of attempts have been made to explain the magnetic susceptibility of curium dioxide with theory. Using DFT, the ground state for curium dioxide is ferromagnetic, which leads to much greater magnetic moments than observed, as shown by Hou et al. Other explanations include mixing of the excited states into the ground state by the crystal field, which was suggested by Morss, et al. The effect of a large crystal field was explored by Niikura and Hotta who found that the observed magnetism could be explained if the crystal field were 10 times larger than that of UO_2. Despite all of these studies, the origin of the temperature-dependent magnetic susceptibility of curium dioxide remains elusive.

Summary: Challenges for theory

One goal of the workshop was to identify areas where theory can greatly aid our understanding of experimental results and guide further experiments. For single molecule magnets, theory has greatly improved the understanding of the tunneling relaxation mechanism due to vibronic coupling in excited states. This insight has been used to design SMMs with better performance by modifying specific vibronic

relaxation pathways. An equally important relaxation pathway that is less well understood is QTM, which allows the ground state to tunnel through the barrier as illustrated in Fig. 2. Part of the challenge to fully understanding QTM is that there are many possible pathways. QTM due to coupling of neighboring spins has been successfully modeled by Aravena. Molecular symmetry is also expected to play an important role in preventing QTM, as reported by Liu et al. Certain symmetries, including D_{5h}, are expected to eliminate QTM. However, this postulate is not entirely consistent with experimental results. Guo et al. reported the performance of a Dy SMM that has almost perfect D_{5h} symmetry; however, this molecule displays very strong QTM. On the other hand, the $N_2^{3-\bullet}$ radical-bridged, Dy_2 complex reported by Rinehart et al. has very low symmetry but displays little QTM. Any improvement in understanding the relationships between the properties of molecules and QTM would be extremely helpful in guiding novel SMM syntheses. This is certainly one area where theory will greatly aid the field of single-molecule magnetism.

The other area where theory can make important contributions is the magnetism of Cm^{4+} compounds. As noted above, the magnetic behavior of this ion is puzzling. From the known magnetism of Cm^{4+} compounds, it is not even clear if this ion has the expected singlet ground state. In addition to computational studies, further experiments are needed especially for determining the effects of radiation damage on magnetic susceptibilities.

Acknowledgments

I thank Corwin H. Booth and Norman M. Edelstein for many helpful discussions on the electronic structures and magnetic behavior of actinide and lanthanide complexes. This work was supported by US Department of Energy, Basic Energy Sciences, Chemical Sciences, Biosciences, and Geosciences Division, Heavy Element Chemistry Program and was performed at Lawrence Berkeley National Laboratory under Contract No. DE-AC02-05CH11231.

Further reading:

1. *L. Escalera-Moreno, J.J. Baldovi, A. Gaita-Ariño, E. Coronado "Exploring the high-temperature frontier in molecular nanomagnets: from lanthanides to actinides," Inorg. Chem., 2019, 58, 11883–11892.*
2. *A. Fort, A. Rettori, J. Villain, D. Gatteschi, R. Sessoli "Mixed quantum-thermal relaxation in Mn_{12} acetate molecules," Phys. Rev. Lett., 1998, 80, 612–615.*
3. *C.A.P. Goodwin, F. Otru, D. Reta, N.F. Chilton, D.P. Mills, "Molecular magnetic hysteresis at 60 kelvin in dysprosocenium," Nature, 2017, 548, 439–444.*
4. *F.S. Guo, B.M. Day, Y.C. Chen, M.L. Tong, A. Mansikkamäki, R.A. Layfield, "A dysprosium metallocene single-molecule magnet functioning at the axial limit," Angew. Chem. Int. Ed. Eng., 2017, 56, 11445.*
5. *R. Sessoli, D. Gatteschi, A. Caneschi, M.A. Novak, "Magnetic bistability in a metal-ion cluster," Nature, 365, 141–143.*
6. *R. Sessoli, H.L. Tsai, A.R. Schake, S. Wang, J.B. Vincent, K. Folting, D. Gatteschi, G. Christou, D.N. Hendrickson "High-spin molecules: $[Mn_{12}O_{12}(O_2CR)_{16}(H_2O)_4]$," J. Am. Chem. Soc., 1993, 115, 5, 1804–1816.*
7. *M. Colarieti-Tosti, O. Eriksson, L. Nordstrom, J. Wills, M.S.S. Brooks, "Crystal-field levels and magnetic susceptibility in PuO_2," Phys. Rev. B, 2002, 65, 195102.*
8. *F. Gendron, J. Autschbach "Puzzling lack of temperature dependence of the PuO_2 magnetic susceptibility explained according to ab initio wave function calculations," J. Phys. Chem. Lett., 2017, 8, 673–678.*
9. *L.R. Morss, J.W. Richardson, Jr., C.W. Williams, G.H. Lander, A.C. Lawson, N.M. Edelstein, G.V. Shalimoff, "Powder neutron diffraction and magnetic susceptibility of $^{248}CmO_2$," J. Less Comm. Met., 1989, 156, 273–289.*
10. *A.B. Shick, J. Kolorenč, L. Havela, T. Gouder, and R. Caciuffo "Nonmagnetic ground state of PuO_2," Phys. Rev. B, 89, 041109.*

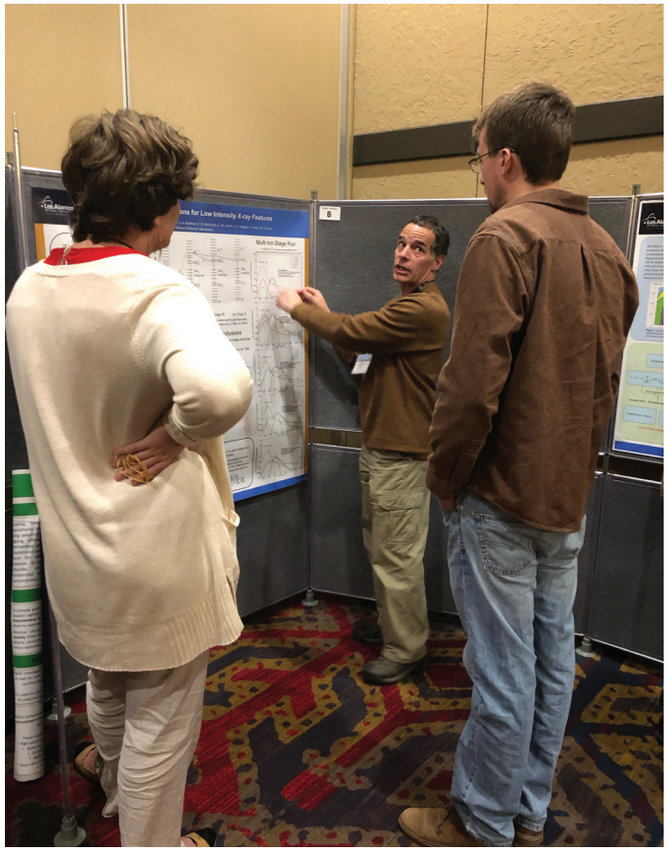

International workshop on

Theory Frontiers in Actinide Sciences: Chemistry and Materials

Santa Fe, New Mexico

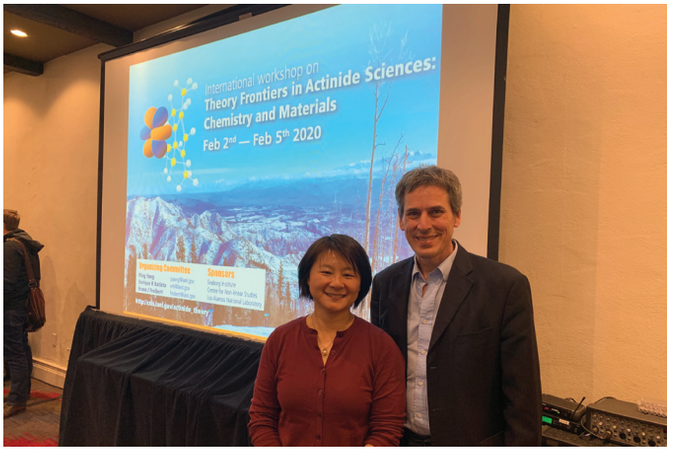

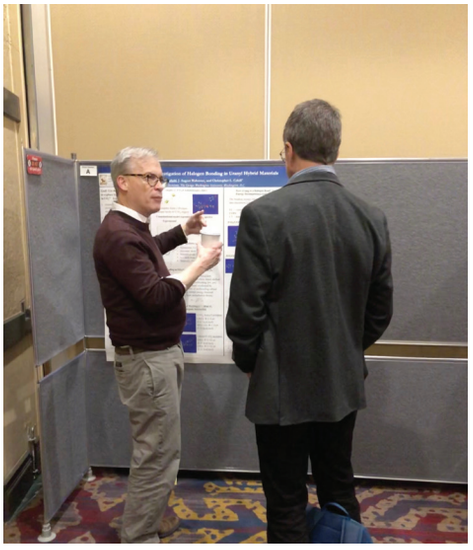

THE GLENN T. SEABORG INSTITUTE

Center for Nonlinear Studies

Los Alamos NATIONAL LABORATORY EST.1943

How Surface Chemistry Affects Spent Nuclear Fuel

Gaoxue Wang, Enrique R. Batista, Ping Yang
Los Alamos National Laboratory, Los Alamos, New Mexico

The fluorite-structured actinide dioxides (AnO_2, particularly UO_2) are the most commonly used fuels in nuclear reactors. Understanding the surface chemistry of the AnO_2 series therefore is of both fundamental and technological importance. Many fundamental questions relating to AnO_2 surface chemistry need answering for the safe processing, recycling and reuse, long-term storage, and environmental effects of nuclear fuels. Examples of issues relevant to the surface properties of these materials include the atomistic description of AnO_2 surface structures, the stability of different surface planes, the effect of defects on the properties of AnO_2 surfaces, and the mechanisms of interaction between environmental molecules and AnO_2 surfaces. However, our understanding of AnO_2 surface chemistry has been so far limited by the difficulties associated with the handling of radioactive actinides in experiments. The computational approaches for the atomic simulation of surfaces have reached a state of maturity such that modeling studies can now supplement experimental efforts.

Limits of actinide dioxide knowledge

Our knowledge of AnO_2 surface chemistry is limited primarily due to two factors. First, specialized laboratory equipment is required to handle actinides experimentally because these elements are radioactive. Early actinides such as thorium and uranium are relatively abundant in nature and their most stable isotopes have long radioactive decay times, making them appropriate for laboratory work. The highly radioactive transuranic elements meanwhile have shorter lifetimes and are therefore not found in nature; they are produced artificially and are only available in small quantities. Accordingly, most experimental studies of AnO_2 surfaces have focused on UO_2, leaving the remainder of the AnO_2 series comparatively unexplored. Experimental studies of single-crystallized materials of transuranic oxides are particularly rare in the literature.

The second reason for our limited understanding of AnO_2 surface chemistry is that we lack characterization techniques with sufficient precision at the atomic scale. Most of the methods used to probe surface properties, such as X-ray photoelectron spectroscopy (XPS) and Auger Electron Spectroscopy (AES), have penetration depths varying from a few nanometers to micrometers, and the signals from these techniques typically represent an average over these depths. Directly observing the atomic surface structure and chemical properties of AnO_2 surfaces using these experimental techniques is challenging without help from atomistic simulations.

Driven by the experimental difficulties studying AnO_2 surfaces and the improvement in computational power and methodology, the last few years have seen extensive efforts to simulate AnO_2 surfaces using ab-initio electronic structure calculations. However, treatment of actinides using density functional theory (DFT) remains non-trivial due to a combination of factors not present in the lighter elements of the periodic table, e.g.: relativistic effects, strongly-correlated 5f electrons, and noncollinear magnetism. Different approaches have been proposed to circumvent this problem of standard DFT functional. One of the most popular methods is

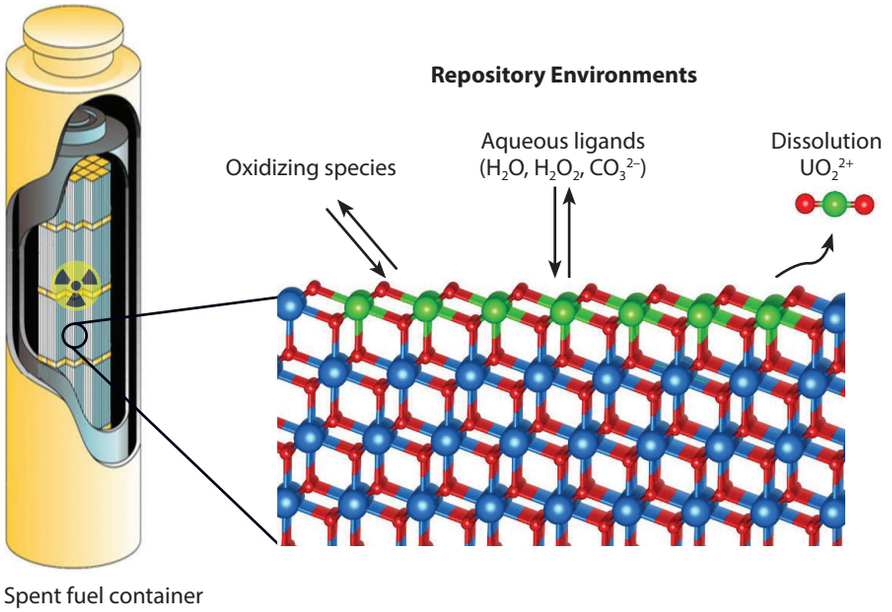

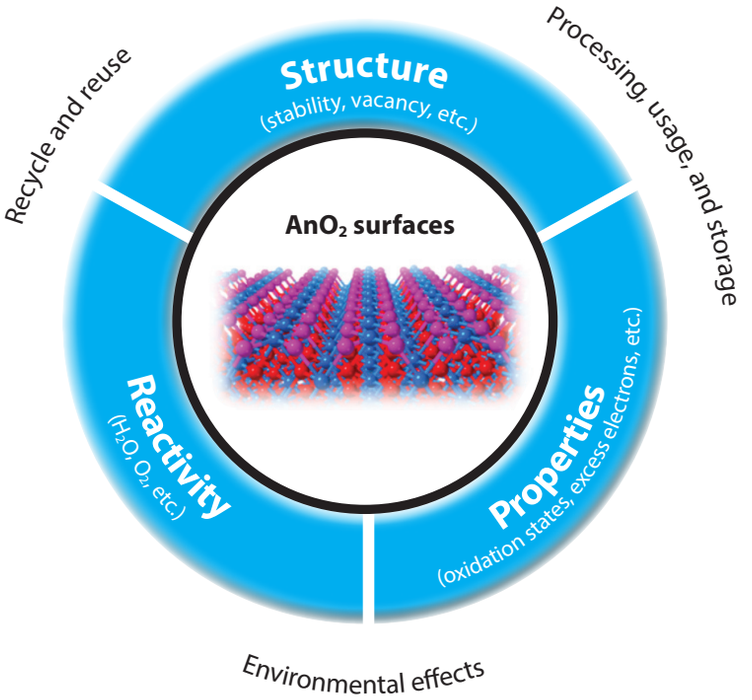

Figure 1. Surface chemistry of actinide dioxides.

DFT+U, which involves the introduction of an empirical Hubbard U correction term to the Hamiltonian. This method has been widely used because it does not increase the computational cost and it can greatly improve the description of the 5f electrons. Here, we present two examples demonstrating the importance of atomic simulations in understanding AnO_2 surface chemistry using DFT studies. The first study focuses on controlling the surface energy of different AnO_2 planes to tune the morphology of AnO_2 nanoparticles. The second shows the critical effect of surface electronic structure on the reactivity of AnO_2 surfaces using water splitting as an example.

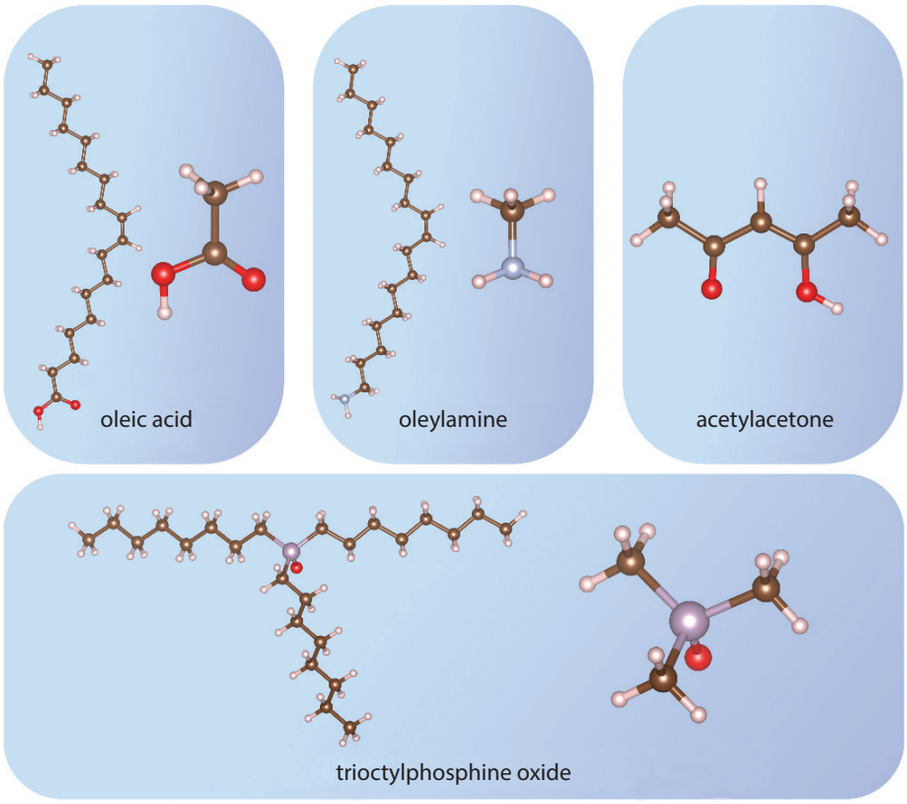

Figure 2. Organic ligands used to synthesize ThO_2 nanocrystals. In our simulations, smaller ligands with the same functional group were used to mimic the ligands with long tails to reduce computational costs.

Ligand-induced shape transformation of ThO_2 nanocrystals

Nanocrystals with size- and shape-dependent properties are of great scientific interest. Remarkable progress has been made in the controlled synthesis of nanocrystals of stable elements in the past two decades, however, our knowledge of actinide nanocrystals has been considerably limited due the difficulties described above. Recently, a non-aqueous surfactant-assisted synthesis has been used for the preparation of actinide oxide nanocrystals (ThO_2, UO_2, and NpO_2), yielding structures with different morphologies such as branched nanocrystals, nanodots, and nanorods. The nanocrystals were synthesized in a mixture of organic molecules including oleic acid, acetylacetone, oleylamine, and trioctylphosphine oxide (Fig. 2). However, both the underlying mechanism that controls the morphologies and the role of different ligands in nanocrystal growth are unclear.

In order to understand the role of ligands in ThO_2 growth we performed a DFT study on ThO_2 surfaces and their interactions with different surfactant ligands. The low Miller index (111), (110), and (100) lattice planes were considered because their surface energies span a wide range, thus they can represent most surfaces of ThO_2 (see the explainer of Miller indices on the opposite page). The thermodynamic stability of ThO_2 nanocrystals in different shapes was then evaluated employing a modified Wulff construction as a thermodynamic model. Ligand molecules with long tails were represented using smaller ligands with the same functional group to maintain the same chemistry with reduced computational costs; specifically, we used acetic acid ($C_2H_4O_2$) to represent oleic acid ($C_{18}H_{34}O_2$). It was found that the (111) surface of ThO_2 has the lowest surface energy among the studied models, therefore pristine ThO_2 nanocrystals will tend to grow in an octahedral geometry terminated by (111) planes (Fig. 3).

Miller indices

Miller indices (hkℓ) form a notation system in crystallography for planes in crystal lattices, where h, k, and ℓ are integers and correspond to the three dimensions x, y, and z. This describes a plane which is orthogonal to the reciprocal lattice vectors (hkℓ). In practical terms, (hkℓ) denotes a plane that intercepts the three axes at a_1/h, a_2/k, and a_3/ℓ. A plane which does not intersect the axis has an "a" value of infinity, therefore its reciprocal is zero. E.g., the (111) plane crosses the x, y and z axes at a point of 1 from the origin.

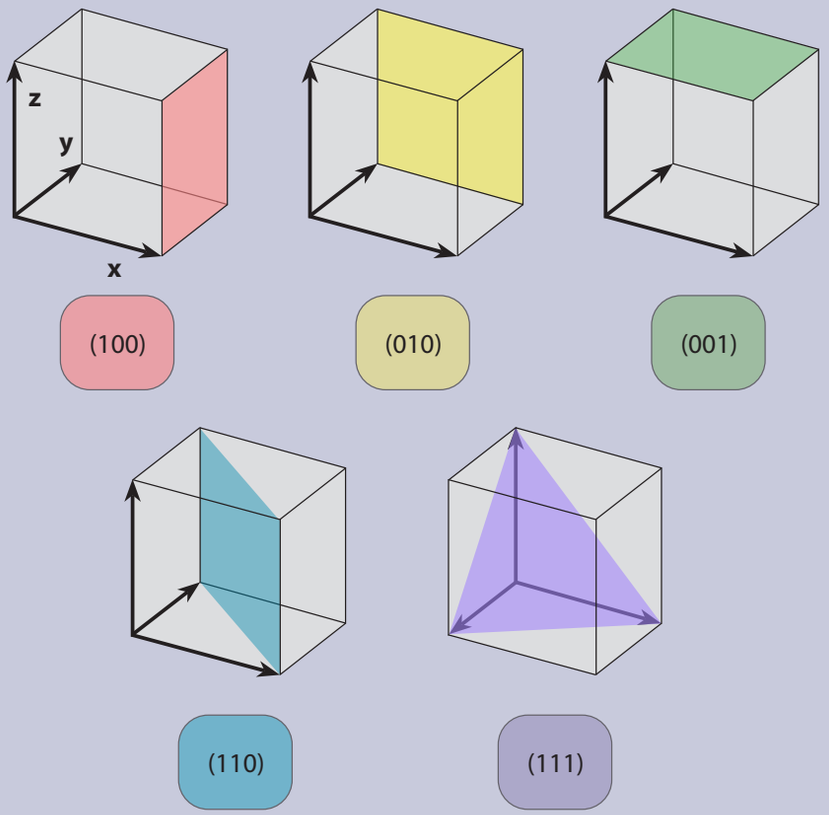

The adsorption of ligands can significantly affect the surface energy for different facets, in turn altering the morphologies of ThO_2 nanocrystals due to selective adsorption on different surfaces. In particular, molecules with carboxylate group (–COOH) display stronger affinity for the (110) surface (Fig. 4). The selective adsorption of acetic acid on the (110) surface is attributed to the differences in the surface structures—Th atoms on the (110) surface have a lower coordination number than on the (111) surface, allowing the ligands to bind more strongly. Moreover, the (110) surface has a flat exterior with Th and O atoms on the same plane, while the topmost layer of (111) and (100) surfaces show the O atoms creating stronger repulsion between the ligand/carboxylate O atoms and the surfaces.

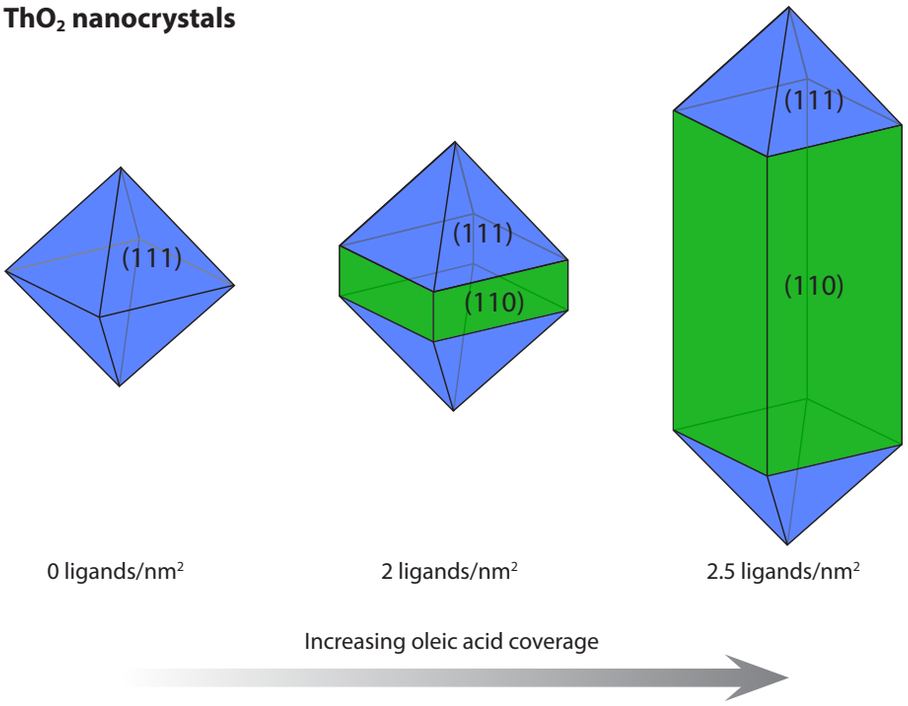

Figure 3. Morphology evolution of ThO_2 with the coverage of oleic acid on surfaces.

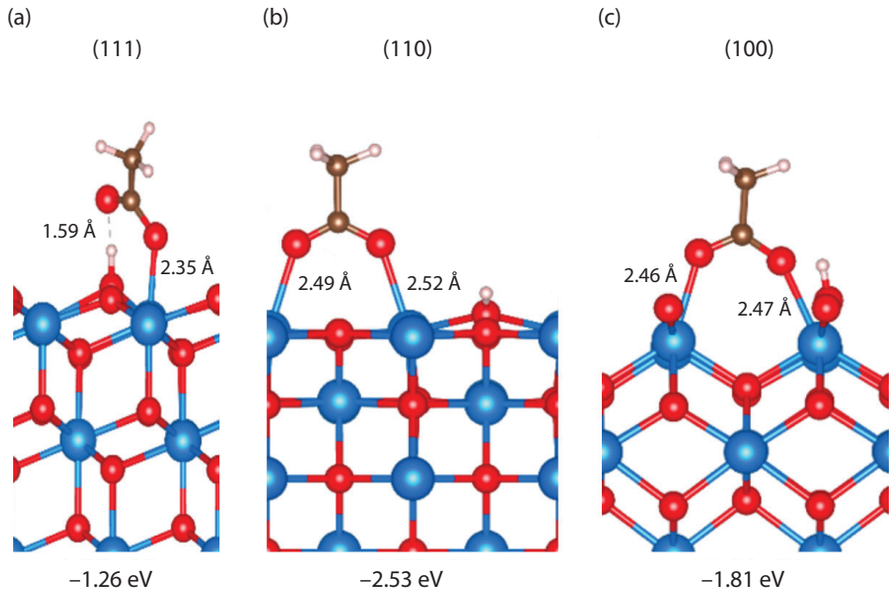

Figure 4. Adsorption configurations and the corresponding binding energies of acetic acid (to represent molecules with carboxylate group) on (a) (111), (b) (110), and (c) (100) surfaces of ThO_2.

The adsorption of ligands can stabilize the growth of different ThO_2 surfaces. The more stable surface will grow as the nanocrystal forms, changing the shape, for instance, from octahedral to nanorod in the case of increasing coverage of oleic acid (Fig. 3). Interestingly, other ligands such as acetylacetone, oleylamine, and trioctylphosphine oxide do not modify the equilibrium shape of ThO_2 nanocrystals. These calculations highlight the critical role of surface-ligand interactions in determining the nanocrystal morphology and may pave the way towards a comprehensive understanding of the formation and growth of other AnO_2 nanocrystals with well-defined sizes and shapes for future applications.

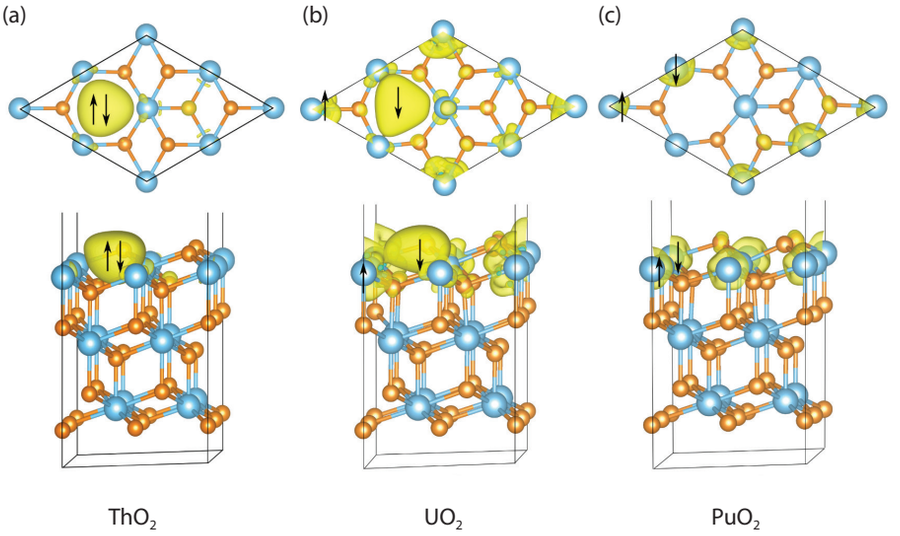

Figure 5. Partial charge density for (a) ThO_2, (b) UO_2, and (c) PuO_2 (111) surfaces with an oxygen vacancy. The arrows represent the spin-up/spin-down electrons due to the oxygen vacancy.

Water splitting on AnO_2 surfaces with oxygen vacancies

The interaction of water with AnO_2 compounds has attracted a great deal of interest due to its importance in corrosion studies of nuclear fuels. It has been shown that the adsorption of H_2O molecules on the perfect UO_2 (111) surface is reversible at 300 K, indicating that H_2O is weakly adsorbed. In contrast, when oxygen vacancies are present, H_2O strongly interacts with the (111) surface and can split into H_2. Nonetheless, our understanding of the electronic structure and catalytic properties across the AnO_2 surfaces is still lacking, especially with respect to surfaces with oxygen vacancies, and the effects of these vacancies on actinide oxidation states and surface chemical reactions.

Motivated by the aforementioned questions, computational modeling was used to study the electronic structure and water splitting chemistry of ThO_2, UO_2, and PuO_2 (111) surfaces with oxygen vacancies. Because of the formally O^{2-} state of oxygen in these materials, each oxygen vacancy leaves two excess electrons on the surface (we use the term "formal" in chemistry to describe integral electron counting in a molecule). We found that these excess electrons distribute differently depending on the actinide involved (Fig. 5). On the ThO_2 surface, the electrons remain at the vacancy site and form a lone pair. At the other extreme, excess electrons localize on two Pu centers on the PuO_2 surface, and consequently reduce their oxidation state from Pu^{4+} to Pu^{3+} (i.e., each Pu center has formally gained an electron). In contrast, on the UO_2 surface, one of the excess electrons remains at the vacancy site and the other is located in a 5f orbital of a neighboring uranium ion.

The differences in the distribution of excess electrons can be explained by the contraction and energy decrease of the 5f orbitals from Th to Pu: the 5f orbitals of Pu are lower in energy than the vacancy states and therefore favor reduction of the metal centers, whereas in Th, the 5f orbitals are much higher in energy, hindering the reduction. The change in electronic structure from ThO_2 to PuO_2 surfaces with oxygen vacancies leads to different chemical properties and reactivity of the AnO_2 surfaces. We have demonstrated this in our studies of the splitting of H_2O catalyzed by ThO_2, UO_2, and PuO_2 (111) surfaces. On stoichiometric surfaces, the formation of H_2 from catalytic splitting of H_2O is endothermic (i.e., energy-absorbing) for all three AnO_2 (111) surfaces evaluated. In contrast, the H_2O splitting reaction and H_2

production is spontaneous in the presence of oxygen vacancies. The ThO_2 surface shows the most exothermic (energy-releasing) reaction process with small energy barriers. This is due to a lone electron pair at the vacancy site on ThO_2 (Fig. 5a) that can readily participate in chemical reactions with H_2O. Meanwhile, on the PuO_2 surface, there is a larger energy barrier for the H_2 production, although the H_2O adsorption and H_2 production is energetically preferred.

Summary

Understanding actinide dioxide surface chemistry is relevant to many stages in the nuclear industry and significant work has been performed in the research community to explore the properties and reactivity of AnO_2 surfaces. In combination with experimental results, atomic simulations can provide insights into electronic structure and chemical reactions on the AnO_2 surfaces. Our recent work has demonstrated the significant role of ligand-surface interactions in the determination of ThO_2 nanocrystal morphology, in addition to vacancy formation and its impacts on catalyzing the production of H_2 on AnO_2 surfaces. Oxygen vacancies are expected to be present on the surfaces of spent nuclear fuels due to radiation damage. If spent fuels are exposed to water in a geological storage facility it will therefore lead to the production of H_2. The accumulation of H_2 can cause the pressurization of the fuel containers, which is a serious safety issue to consider for long-term storage of spent nuclear fuels.

Acknowledgments

The authors gratefully acknowledge funding from the Laboratory Directed Research and Development program of Los Alamos National Laboratory (LANL) under project 20160604ECR 20180007DR, and US DOE office of Basic Energy Science under the Heavy Element Chemistry program at LANL. The calculations were performed using EMSL (grid.436923.9), a DOE Office of Science User Facility sponsored by the Office of Biological and Environmental Research. G.W. also acknowledges a Director's Postdoc Fellowship from LANL.

Further reading

1. *B. Dorado, et al., "DFT+ U calculations of the ground state and metastable states of uranium dioxide," Phys. Rev. B, 2009, 79, 235125.*
2. *G. Jomard, et al., "Structural, thermodynamic, and electronic properties of plutonium oxides from first principles," Phys. Rev. B, 2008, 78, 075125.*
3. *B. Himmetoglu, et al., "Hubbard-corrected DFT energy functionals: The LDA+ U description of correlated systems," Int. J. Quantum Chem., 2014, 114, 14–49.*
4. *G. Wang, E.R. Batista, P. Yang, "Ligand induced shape transformation of thorium dioxide nanocrystals," Phys. Chem. Chem. Phys., 2018, 20, 26, 17563–17573.*
5. *X.-Y. Liu, D. Andersson, B. Uberuaga, "First-principles DFT modeling of nuclear fuel materials," J. Mater. Sci., 2012, 47, 7367–7384.*
6. *G. Wang, E.R. Batista, P. Yang, "Excess electrons on reduced AnO_2 (111) surfaces (An = Th, U, Pu) and their impacts on catalytic water splitting," J. Phys. Chem. C, 2019, 123, 50, 30245–30251.*
7. *D. Hudry, et al., "Non-aqueous synthesis of isotropic and anisotropic actinide oxide nanocrystals," Chem. Eur. J., 2012, 18, 8283–8287.*
8. *D. Hudry, et al., "Controlled synthesis of thorium and uranium oxide nanocrystals," Chem. Eur. J., 2013, 19, 5297–5305.*
9. *A.S. Barnard, P. Zapol, "A model for the phase stability of arbitrary nanoparticles as a function of size and shape," J. Chem. Phys., 2004, 121, 4276–4283.*
10. *S. Senanayake, H. Idriss, "Water reactions over stoichiometric and reduced UO_2 (111) single crystal surfaces," Surf. Sci., 2004, 563, 135–144.*

Modeling Actinide Surface Chemistry Using Semi-Empirical Methods

Nir Goldman
Lawrence Livermore National Laboratory, 7000 East Ave., L–285, Livermore, California

Plutonium metal is known to have six allotropes between ambient and melting conditions, which yields a wide range of different physical and chemical properties. The metastable face-centered-cubic (fcc) δ-phase is of particular interest for engineering applications in part due to its high ductility and malleability. This phase is highly sensitive to corrosion from adsorbed atmospheric gases, which presents significant challenges because these compounds are ubiquitous in experimental setups. Surface hydrogenation in particular is problematic, in which the Pu-hydride product can spontaneously form and can accelerate strongly exothermic oxidation reactions and even undergo spontaneous ignition. Despite these issues, relatively little is known about pertinent surface chemistry; experimental studies would greatly benefit from detailed atomic-level knowledge of the chemical reactivity of hydrogen on the surface of these systems.

Accurate modeling of the breaking and forming of bonds in condensed phases frequently requires quantum simulation approaches, such as Kohn-Sham Density Functional Theory (DFT). These calculations are extremely computationally intensive, however, and are generally limited to exceedingly small system sizes and timescales. In particular, f-electron solids such as plutonium can be difficult to model efficiently because of the high computational effort associated with these materials. Our previous DFT calculations for hydrogen surface reactivity on δ-Pu crystalline surfaces yielded insight into plutonium corrosion, but were somewhat limited in scope due to the extreme computational costs which precluded the calculation of important time-dependent dynamics, reaction barriers, and other relevant properties. Therefore, a strong need exists for atomistic simulation approaches that can achieve acceptable breadth and accuracy while exhibiting a high degree of computational efficiency.

To this end, we have created a density functional tight-binding (DFTB) semi-empirical quantum approach for the hydrogen/δ-Pu system. Briefly, the method assumes neutral, spherically symmetric charge densities on the atoms and expands the Kohn-Sham DFT Hamiltonian to second-order in charge fluctuations. The DFTB total energy is expressed as the sum of energy terms: E_{BS} (band structure energy), E_{Coul} (charge fluctuation), and E_{Rep} (repulsive energy). The E_{BS} and E_{Coul} terms yield an approximate quantum mechanical treatment of the electrons, whereas E_{Rep} is generally taken to be an empirical, short-ranged function that is fitted to experimental or high-level quantum data. This combination of approximate quantum mechanics and empirical functions allows for several orders of magnitude improvement in computational efficiency over standard quantum approaches while retaining most of their accuracy.

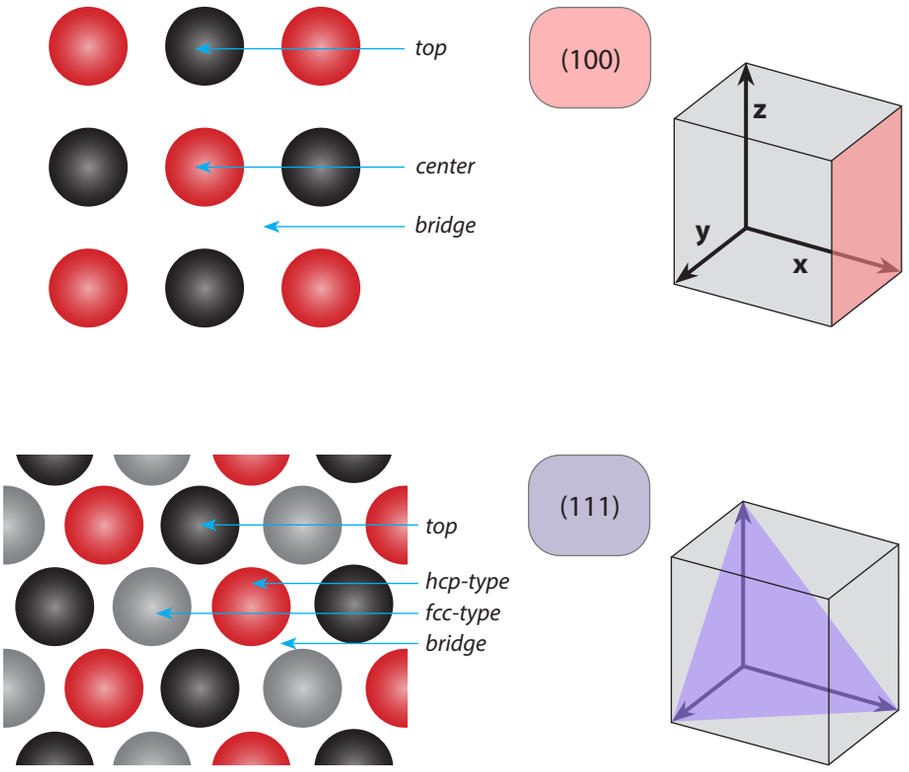

Figure 1. Renderings of the bare δ-Pu (100) and (111) surfaces, with labels for commonly identified adsorption sites. Here, plutonium atoms residing in the surface layer are colored black, atoms in the first subsurface layer are red, and those in subsequent layers are gray.

We leveraged previous quantum results for the hydrogen/δ-Pu system to determine a DFTB model for hydrogen adsorbed onto the (100) and (111) δ-Pu surfaces (these numeric indices correspond to different crystalline facets that are likely to be exposed when a surfaces is formed or cut out of solid δ-Pu, see p27 for a short primer). Optimal parameters for the DFTB plutonium quantum mechanical interactions were chosen after comparing them with the total electronic density of states (DOS) from DFT computed for the optimized δ-Pu bulk system. We determined the repulsive energy term E_{Rep} for the hydrogen-plutonium system through tuning to previous DFT calculations for hydrogen surface adsorption. Notably, we used the recently developed classical force field referred to as the Chebyshev Interaction Model for Efficient Simulation ("ChIMES") to determine our E_{Rep} for this system. This gives an efficient method to include greater than two-body interactions in DFTB calculations, which can be underrepresented in these models. Our approach provided a straightforward and accurate method for performing quantum calculations with significantly smaller computational costs.

Modeling hydrogen chemistry on δ-plutonium surfaces

We tested the accuracy of our ChIMES/DFTB model by first computing the adsorption energetics of single hydrogen molecules and ions on the δ-Pu (100) and (111) surfaces (shown in Fig. 1). In general, our results for the adsorption energies and hydrogen distances from the Pu surface agree well with the spread of numbers from previous spin polarization and DFT calculations. Our DFTB calculations used stricter convergence criteria and improved sampling over the DFT results. Consequently, subtle but important differences between these calculations were observed; for example, we found that the on the (100) surface, the H_2 molecule preferentially adsorbs in the center site with an energy of +0.02 eV (slightly endothermic), compared to a value from DFT of –0.04 eV (exothermic).

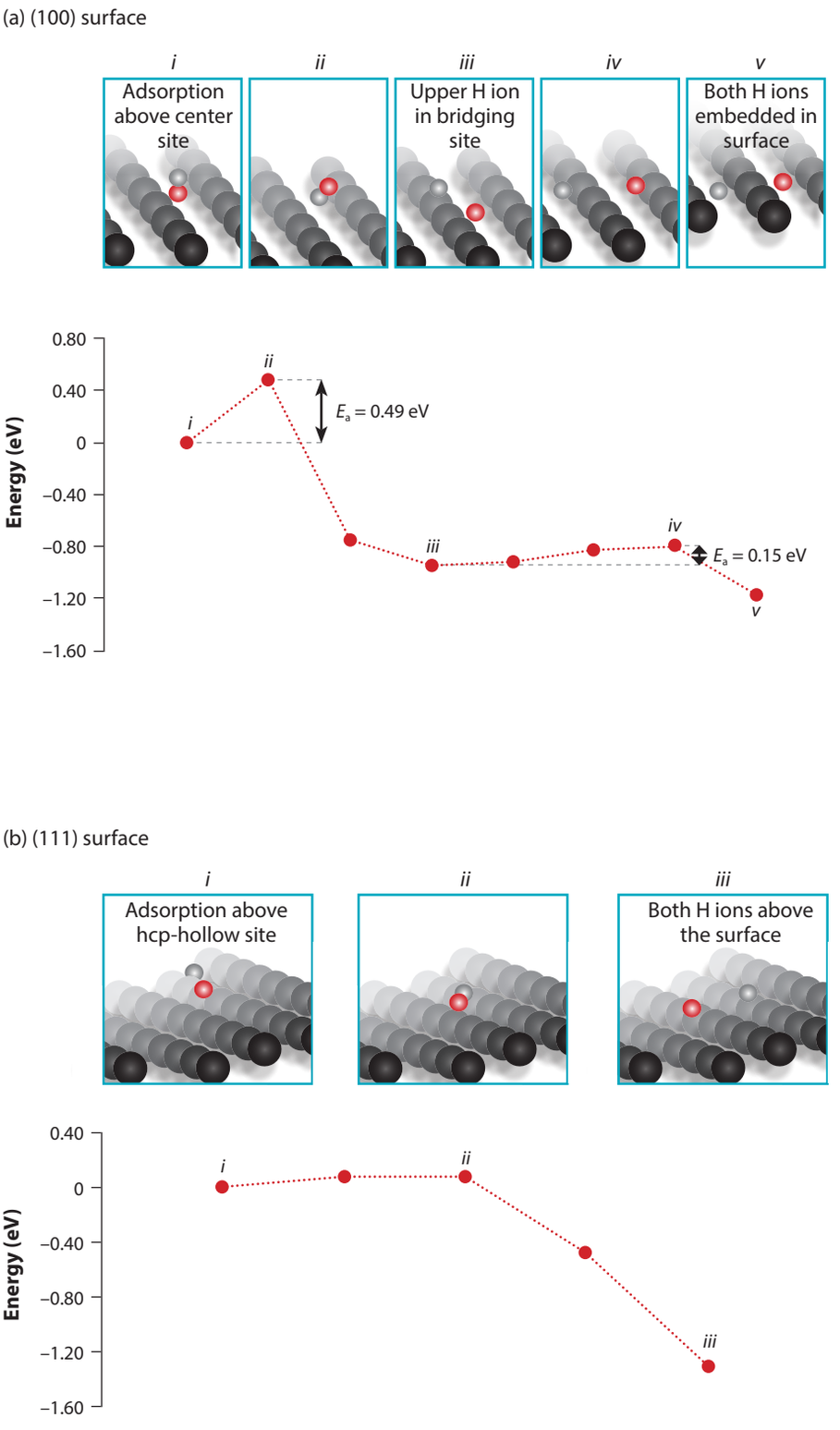

Figure 2. Minimum energy pathways for H_2 dissociation. The hydrogen atom initially closer to the Pu surface is colored red for clarity. For the (100) surface, the final state indicates both hydrogen ions adsorbed on the plutonium surface. In contrast, the energetic barrier for dissociation on the (111) surface is significantly lower, and the hydrogen ions remain slightly above the plutonium surface.

Determining the dynamic properties of the system

In order to examine the dynamic properties of our model, we computed molecular dynamics (MD) trajectories at 298 K to determine the vibrational spectrum for a H_2 molecule adsorbed on either the (100) or (111) surface. Our calculations yielded approximately 0.75 picoseconds of simulation time per day of computer use (ps/day) for the (100) system and 1.25 ps/day for the (111) system on only 12 computing processors (i.e., CPUs). We computed total trajectories of up to 10 picoseconds (ps) for each system. For the sake of comparison, we also computed a DFT-MD trajectory for the (111) system; in contrast, this yielded only 0.100 ps/day and required using 288 CPUs, resulting in a trajectory of less than one ps in total after ten days of computing time. This corresponds to an increase in computational efficiency of 10^{-2}–10^{-3} for our DFTB model, similar to previous efforts.

Our results indicate that on the (100) surface, the H_2 bond remains intact for at least some of the MD trajectory, as suggested by the peak at ~4300 cm^{-1}. In contrast, on the (111) surface the hydrogen molecule experiences rapid dissociation, revealed by the absence of this vibrational mode. The spectrum from this surface also shows a slight blue-shifting of the H–Pu mode at ~380 cm^{-1}, indicative of a slightly stronger H–Pu interaction due to the dissociation of the H–H bond. This result from DFTB compares well to the DFT calculations, in which the H–Pu peak was predicted at ~280 cm^{-1}. We did not observe a H–H stretching mode from DFT on the (111) surface. The discrepancy in the H–Pu peak corresponds to an energy difference of only 0.015 eV and is likely due in part to the poorly converged DFT-MD result. We computed an average H atom/surface distance of 3.62 and 3.12 Å for the (100) and (111) surfaces, respectively. The closer proximity of the molecule to the (111) surface likely contributes to its enhanced dissociation rate for this system.

Modeling surface dissociation and sub-surface diffusion

In order to predict the chemical reaction details of plutonium hydride formation, we computed kinetic pathways (also known as minimum energy pathways, MEPs) for surface dissociation and sub-surface diffusion using the climbing image nudged elastic band (NEB) approach. Analysis of the dissociation MEP on the (100) surface (Fig. 2) indicates a rate-limiting step (activation energy 0.49 eV) in which the H_2 molecule experiences a rocking motion before settling into a first minimum. Here, one hydrogen ion is adsorbed onto the (100) surface center site, and the second hydrogen ion adsorbed in a bridge site (i.e., between surface Pu atoms, approximately 1.20 Å above). The hydrogen ions then experience an additional rocking motion with a small barrier (0.15 eV) before settling into the final state where both hydrogen ions are embedded within the center sites. These values are similar to our DFT estimates.

Our calculations for the adsorption of an undissociated H_2 molecule on the (111) surface yielded a slightly different geometry and adsorption energy compared with DFT values. We computed a small dissociation barrier of only 0.06 eV, which is commensurate with our MD results, and a total reaction energy of –1.30 eV, similar to our DFT calculations (–0.95 eV). The difference is likely due to the improved convergence criteria used in our DFTB calculations, as well as the approximate nature of the energy grid calculation in the DFT result, in which hydrogen ions were placed in arbitrary positions on the Pu surface, rather than computing the NEB pathway.

Finally, we computed the MEPs for hydrogen ion subsurface diffusion on both δ-Pu surfaces, which corresponds to the essential first steps in plutonium hydride formation. On the (100) surface, we observed an endothermic activation energy for the initial adsorption reaction, which leads to a stable intermediate state (Fig. 3).

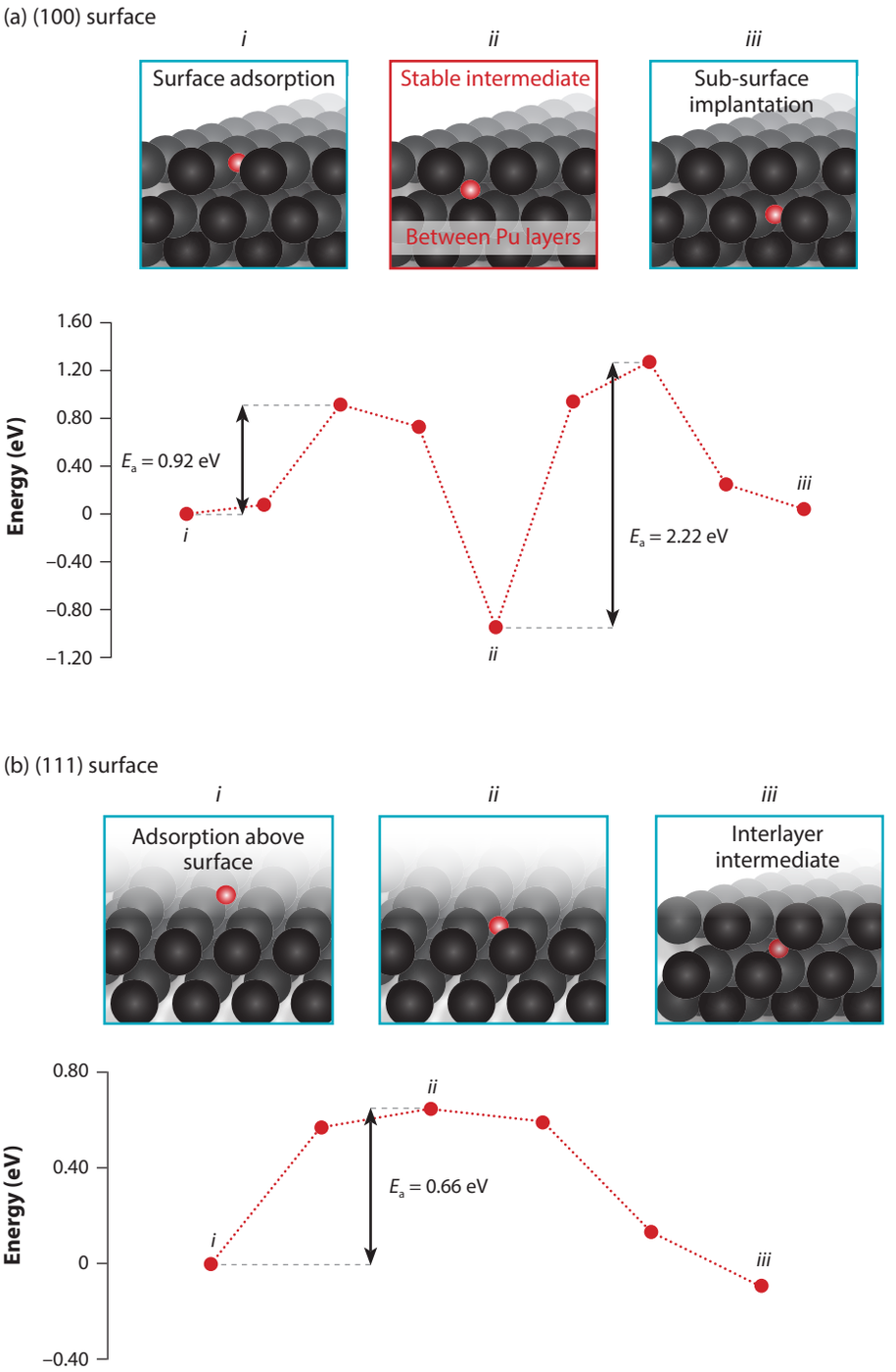

Figure 3. Minimum energy pathways for H ion diffusion to subsurface layers on each plutonium surface. The asymmetric minimum energy pathway for the (100) surface is due to relaxation of the first two Pu layers in initial geometry optimization.

The high negative energy for the intermediate configuration (–0.94 eV) is a result of the tetrahedral coordination of the hydrogen ion by four Pu atoms. This ion faces a comparatively high activation barrier in order to diffuse into the first sub-surface layer. In contrast, on the (111) surface, the hydrogen ion experiences a relatively small activation energy, with a transition state where the H ion is coincident with the surface. These types of results can be used to determine ab initio kinetic Monte Carlo models for surface corrosion, where libraries of possible reactions can easily be built due to the periodic nature of the crystalline slab and the relative simplicity of hydrogen reactivity for this system.

Summary

In this work, we have created a new model for hydrogen reacting with δ-Pu surfaces, using the density functional tight-binding (DFTB) method combined with the Chebyshev Interaction Model for Efficient Simulation (ChIMES). This yielded accurate results for the bulk δ-Pu electronic density of states, an important parameter for predicting material properties, in addition to the approximate H_2 dissociation potential energy surface computed previously by DFT. We have calculated both the vibrational spectra for H_2 adsorbed on different surfaces and the kinetic pathways for the dissociation reaction on each surface, in which we observed somewhat complex reaction paths. We also determined kinetic pathways for sub-surface diffusion of the hydrogen ion and found that the (100) system is possibly less prone to plutonium hydriding due to the presence of a stable, tetrahedrally-coordinated inter-layer intermediate. Our ChIMES/DFTB approach was able to retain the majority of the accuracy of DFT calculations with several orders of magnitude improvement in computational efficiency. Our models can then be used to generate essential inputs for macroscopic models, such as kinetic data, which can be employed to simulate material aging and degradation (among other properties) that are extremely challenging to determine with standard quantum calculation approaches alone.

Acknowledgments

This work was performed under the auspices of the US Department of Energy by Lawrence Livermore National Laboratory (LLNL) under Contract DE-AC52-07NA27344. Computations were performed at LLNL using the borax and quartz massively parallel computers. The project 16-LW-020 was funded by the Laboratory Directed Research and Development Program at LLNL with N.G. as principal investigator.

Further Reading:

1. *N. Goldman, M.A. Morales, "A first-principles study of hydrogen diffusivity and dissociation on δ-Pu (100) and (111) surfaces," J. Phys. Chem. C, 2017, 121, 17950–17957.*
2. *N. Goldman, B. Aradi, R.K. Lindsey, L.E. Fried "Development of a multicenter density functional tight binding model for plutonium surface hydriding," J. Chem. Theory Comput., 2018, 14, 2652–2660.*

Electron Transfer Reactions at the Nexus of Water, Minerals, and Contaminant Metals

Kevin M. Rosso
Pacific Northwest National Laboratory, 902 Battelle Blvd, Richland, Washington

The chemistry of natural aquatic systems is fundamentally based on electron transfer reactions. This includes inorganic, organic, and biologic processes, which in the natural environment couple together in complex ways to set the prevailing chemical characteristics of the system. At the molecular scale, electron transfer entails a redistribution of charge between reactants during mutual encounter, a redistribution that often breaks or makes new chemical bonds and imparts new properties to the products. These new properties can come in the form of dramatic changes, such as transforming a chemical species from toxic to benign, or from mostly water-soluble to insoluble, leading to nearly instantaneous precipitation of solids.

Reduction and oxidation reactions, or so-called redox reactions, fit into this category. Common metals in the Earth's crust, such as iron and manganese, are redox-active with multiple stable valence states, making them dominant participants in electron transfer reactions in, for example, groundwater. The radioactive element uranium is also redox-active. Although far more rare in nature, enrichment of uranium isotopes for use in nuclear fuel or weapons has, unfortunately, also led to their ultimate release into terrestrial settings, comprising a hazardous contaminant to humans, animals, plants, and microorganisms.

Redox reactions between uranium and iron are critically important for understanding the transport and fate of uranium below ground, particularly with increasing depth as oxygen availability decreases. Near the Earth's surface, its stable form is hexavalent U(VI), found as the aqueous-soluble uranyl cation UO_2^{2+}, which is mobile in oxic groundwaters (i.e., containing dissolved oxygen). But in deeper strata where oxygen is limited and the redox conditions are reducing, the stable form is insoluble U(IV) in which uranium tends to be immobilized in minerals such as uraninite, UO_2 (also known as pitchblende). Iron solubilities, on the other hand, are the opposite. The oxidized form Fe(III) is highly insoluble and exists largely in ferric oxide minerals, whereas the reduced form Fe(II) resides mostly in solution (although minerals such as magnetite containing both Fe(III) and Fe(II) are also common). It should therefore be possible to imagine a redox-transition zone in the subsurface, where oxic pore fluids containing U(VI) intersect with reducing sediments dominated by Fe(II), where the electron transfer reactions between these two metals causes precipitation of U(IV) and Fe(III) solids, effectively immobilizing the uranium in mineralized form.

Electron transfer pathways between iron and uranium are complex

Understanding the pathways for these U(VI)/Fe(II) electron transfer reactions is important for predicting the overall immobilization rate, but in terms of elementary steps at the molecular level this is clearly a complex system. Modern electron transfer

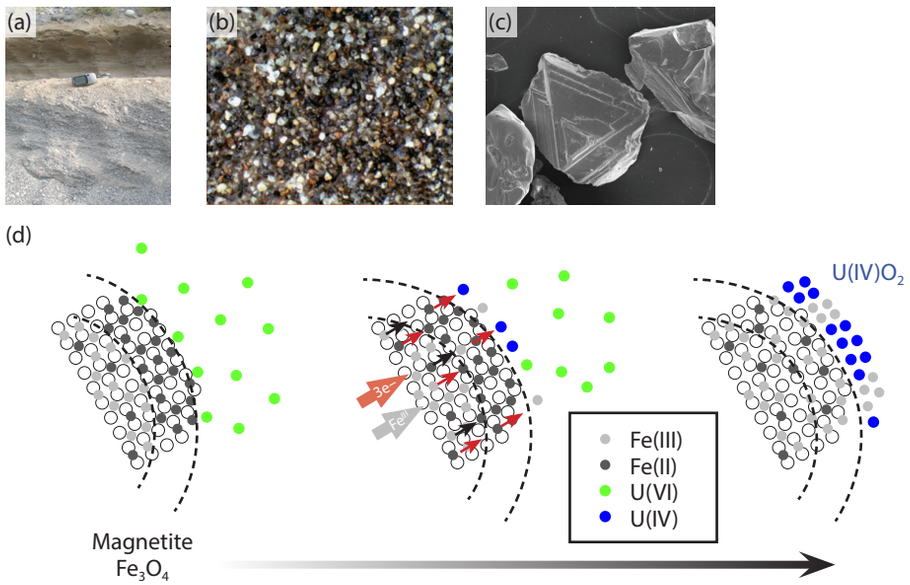

Figure 1. (a) Field example from the Hanford site, Washington, USA of (b) sediments containing Fe(II)-bearing minerals such as that shown by (c) scanning electron micrography to be magnetite grains capable of (d) heterogeneous reduction of U(VI) to U(IV) that occurs by electron transfer across the mineral/water interface.

theory tells us that reduction of U(VI) to U(IV) should proceed by sequential one-electron transfer reactions. So at first glance, two Fe(II) one-electron donors are needed to achieve complete reduction of U(VI) to U(IV) and we can expect that an intermediate U(V) valence state may also be involved. U(V) is rarely found in nature and tends to be considered unstable. However, should conditions arise that favor its accumulation to the extent that U(V) species can encounter each other, mutual one-electron transfer yields U(VI) and U(IV) by so-called disproportionation—this opens a second pathway to the U(IV) reaction product U(IV). Furthermore, because forms of Fe(II) include both aqueous and mineral species, U(VI) reduction can occur both in homogeneous aqueous solution and heterogeneously on surfaces of minerals such as magnetite (Fig. 1). These two mechanisms may have very different intrinsic rates, with the latter tending to catalyze the reaction. In the subsurface where mineral surfaces are abundant, the reduction reaction can occur by both mechanisms simultaneously. Given these complexities, predicting the overall reaction rate is a challenge.

Indeed, there have been many experimental studies showing that both aqueous and mineralogic Fe(II) can reduce U(VI) to U(IV) under environmental conditions. Occasionally, stabilization of intermediate U(V) states has been observed, either as sorption complexes or by incorporation into Fe(III) oxide mineral products. In laboratory studies using homogeneous aqueous solution, because the first appearance of U(IV) in the system triggers metal oxide precipitation the rest of the reduction reaction rapidly cascades to completion. It is thus challenging to determine whether reduction to U(IV) is facilitated by Fe(II) alone, or by rapid disproportionation, or both. Current literature offers mixed conclusions. Although it is typically assumed that Fe(II) can reduce U(VI) to U(V), it remains uncertain whether its reduction potential is strong enough for the subsequent electron transfer to U(IV). Because U(V) complexes have been notoriously difficult to isolate, their elimination by disproportionation has long been considered fast. It is noteworthy that essentially all experimental studies examining the kinetics of homogeneous U(V) disproportionation have necessarily been conducted in extremely acidic conditions (i.e., pH <2) in order to avoid rapid condensation of U(IV). However, in this acidic regime where U(V) is stable, increasing acidity was shown to promote U(V) disproportionation, with the slowest rates observed at the higher end of pH values examined (i.e., pH 2–3). Extrapolation to circumneutral pH suggests that the homogeneous

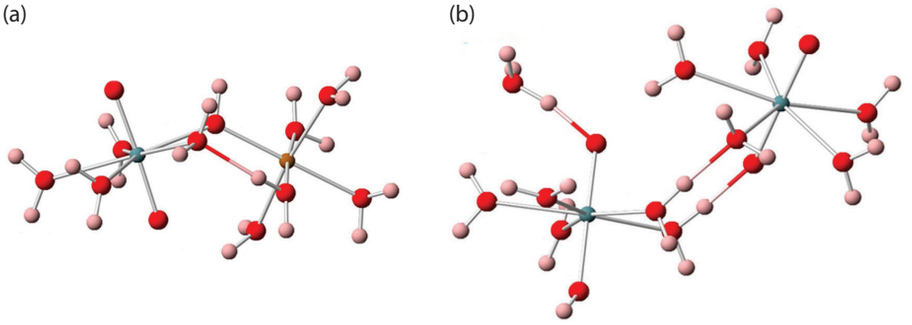

Figure 2. Theoretical electron transfer encounter complexes predicted by density functional theory calculations for: (a) reduction of the first hydrolysis species of U(VI) by Fe(II), and (b) disproportionation of U(V)-U(V) at acidic conditions in which protonation of axial oxygens stabilizes electron transfer to U(IV)-U(VI).

disproportionation pathway under environmental conditions may instead be intrinsically slow, and that rapid elimination of U(V) under these conditions must therefore occur by Fe(II) in a yet to be identified catalytic form, such as a sorbent on precipitating metal oxide surfaces.

Molecular simulation fills some knowledge gaps

Our approach to resolving these unknowns has been to apply computational molecular simulations in the framework of Marcus theory to predict the kinetics of key electron transfer steps. This involves calculation of the reactant structures and transition states, and important quantities like the reaction free energy, reorganization energy, and electronic coupling matrix element. These computer simulations naturally overcome the experimental challenge of unraveling parallel pathways; for instance, we can exclusively focus on specific unresolved aspects of the elimination mechanism for U(V) at circumneutral pH by electron transfer from either Fe(II) or another U(V) complex in homogeneous aqueous solution.

We used density functional theory (DFT) to first compute the structures and total energies of aqueous monomeric U(VI) and Fe(II) species that dominate at environmentally relevant concentrations, e.g., UO_2^{2+} and its hydrolyzed derivatives, and $Fe^{2+}(OH_2)_6$ (0.1 μM U(VI) and 200 μM Fe(II) at pH values ≤ 7). The results show that U(VI) reduction to the U(V) species UO_2^+ by hexaquo Fe^{2+} is thermodynamically favorable but kinetically slow. An essential first step is to model the formation of encounter complexes that enable the electron transfer reaction. Outer-sphere encounter complexes entail intact coordination spheres around each reactant and typically involve longer, and therefore less probable, electron transfer distances, whereas inner-sphere complexes entail the formation of a chemical bridge between the reactants, such as by sharing a hydroxyl group, often facilitating the electron transfer. Although any kind of encounter complex between UO_2^{2+} and $Fe^{2+}(OH_2)_6$ was predicted to be unstable because of mutual electrostatic repulsion, a stable inner-sphere complex was found for the first hydrolysis species $UO_2(OH)^+$, in which electron transfer was predicted to occur at a rate of 4.3×10^3 s^{-1} (Fig. 2a). Likewise, stable inner- and outer-sphere encounter complexes were found for other important U(IV) hydrolysis species with electron transfer rates ranging from 7.6×10^2 to 7.2×10^4 s^{-1}. Therefore, computational chemistry now supports the hypothesis that U(VI) to U(V) reduction by Fe(II) is thermodynamically favorable and relatively fast.

Using the same approach, we found no evidence that U(V) could be further reduced by Fe(II) alone, pointing us instead to the possibility of U(V)–U(V) disproportionation as a route to U(IV). Given that the structural and chemical properties of U(V) are largely unknown, careful consideration of its speciation and possible encounter complexes was essential. Our DFT results are consistent with expectations that the structure of U(V) should be characterized by two axial oxygen atoms akin to

those of U(VI), i.e., the U(V) species UO_2^+. Only one prior theoretical study has been performed on the disproportionation reaction between two of these species, which suggested a relatively slow rate of ~10^{-1} $M^{-1}s^{-1}$, albeit based on an ad hoc U(V)-U(V) encounter complex and without considering the pivotal role of pH. Other modeling studies examined the prospect of inner-sphere "cation-cation" encounter complexes based on their occurrence in certain actinide salts, containing axial oxygen groups at one U(V) center and occupying equatorial coordination sites of the other. However, it has never been shown that such structures spontaneously form in aqueous solution. In contrast, our DFT research showed that while stable U(V)–U(V) encounter complexes could be found, all were outer-sphere, and all associated electron transfer rates were predicted to be insignificant at circumneutral pH.

A critical discovery was that protonation of both axial oxygen atoms at the acceptor U(V) center within the encounter complex stabilizes its conversion to U(IV) (Fig. 2b). Given the extremely acidic character of the axial oxygen groups, our finding is consistent with the experimental observation that the disproportionation reaction is only relevant at extremely low pH in which protonation of axial oxygen groups is possible, and that its reaction rate steadily decreases with increasing pH due to their deprotonation. Thus, computational chemistry suggests that this pathway to U(IV) is also unimportant under environmentally relevant conditions, at least in homogeneous aqueous solution. This is contrary to prevailing notions that the scarcity of U(V) is caused by its rapid elimination via disproportionation.

Summary

From our modeling study we can conclude that in deep subsurface environments the most important reduction pathway to U(IV) is heterogeneous catalysis at mineral surfaces (e.g., Fig. 1d) because the examined electron transfer reactions for homogeneous aqueous solution are predicted to be slow. In contrast to common assumptions, aqueous Fe(II) appears incapable of reducing U(VI) beyond U(V), and U(V) disproportionation in solution is likewise an insignificant electron transfer pathway to U(IV) at environmentally relevant pH. U(IV) must be produced either by reaction with Fe(II) associated with mineral surfaces, or by heterogeneous U(V) disproportionation on these surfaces. This conclusion is consistent with prior experiments that show that Fe(II) contact with U(VI) in solution appears to be initially unreactive, but which rapidly cascades to reaction completion by the eventual first appearance of U(IV)/Fe(III) metal oxide products. The computational molecular simulations were also particularly useful for revealing how acidity facilitates U(V) disproportionation.

These kinds of modeling efforts exemplify the ultimate goal of exploiting modern many-atom simulations at the quantum mechanical level to quantify rates of important electron transfer processes controlling the chemistry of environmental systems. Such a goal is now within reach both in terms of existing theories, computational hardware and codes, meriting a sustained campaign to press forward the science one process at a time.

Further reading:

1. *R.N. Collins, K.M. Rosso "Mechanisms and Rates of U(VI) Reduction by Fe(II) in Homogeneous Aqueous Solution and the Role of U(V) Disproportionation," J. Phys. Chem. A, 2017, 121, 35, 6603–6613, https://doi.org/10.1021/acs.jpca.7b05965.*

THE GLENN T.
SEABORG
INSTITUTE

Actinide Research Quarterly is published by Los Alamos National Laboratory and is a publication of the Glenn T. Seaborg Institute for Transactinium Science, a part of the National Security Education Center. ARQ (est. 1994) highlights research in actinide science in such areas as process chemistry, metallurgy, surface and separation sciences, atomic and molecular sciences, actinide ceramics and nuclear fuels, characterization, spectroscopy, analysis, and manufacturing technologies.

LA-UR-20-26206

Address correspondence to:
Actinide Research Quarterly
c/o Editor
Mail Stop T-001
Los Alamos National Laboratory
Los Alamos, NM 87545

ARQ can be read online at:
www.lanl.gov/arq

If you have questions, comments, suggestions, or contributions, please contact the ARQ staff at:
arq@lanl.gov

National Security Education Center
David L. Clark, Director

G. T. Seaborg Institute for Transactinium Science
Science Advisors
Franz Freibert, Director
Ping Yang, Deputy Director

Editor
Owen Summerscales

Contributing editors
Susan Ramsay

Designers/Illustrators
Don Montoya
Owen Summerscales

Circulation Manager
Susan Ramsay

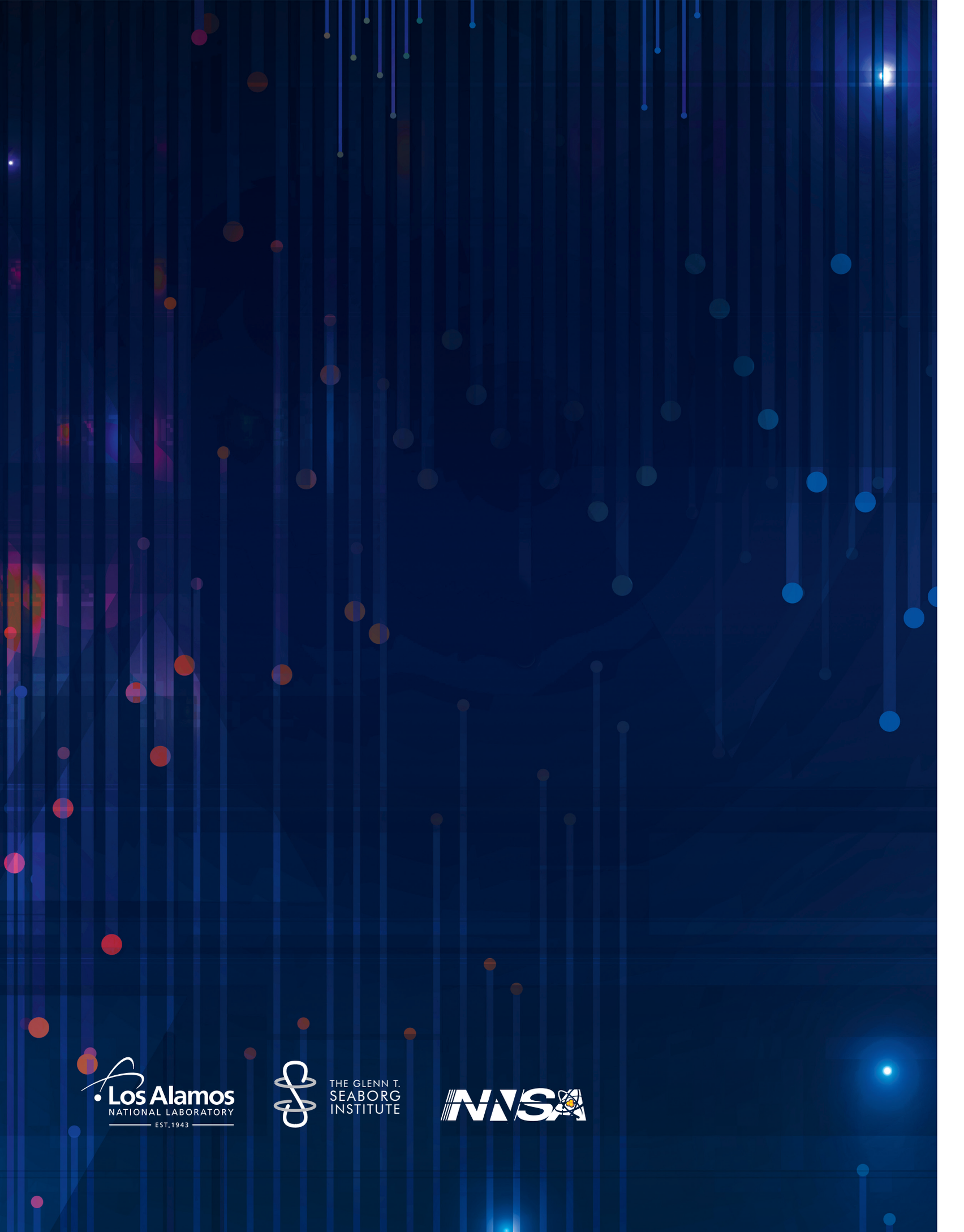
Los Alamos
NATIONAL LABORATORY
EST. 1943
THE GLENN T.
SEABORG
INSTITUTE
NNSA